




# Metastatic Infiltration of Nervous Tissue and Periosteal Nerve Sprouting in Multiple Myeloma-Induced Bone Pain in Mice and Human

 Marta Diaz-delCastillo,<sup>1,2,3,4,5,6</sup> Oana Palasca,<sup>7</sup> Tim T. Nemler,<sup>1</sup> Didde M. Thygesen,<sup>1</sup> Norma A. Chávez-Saldaña,<sup>8</sup> Juan A. Vázquez-Mora,<sup>8</sup> Lizeth Y. Ponce Gomez,<sup>8</sup> Lars Juhl Jensen,<sup>7</sup> Holly Evans,<sup>3,4</sup> Rebecca E. Andrews,<sup>3,4,5</sup> Aritri Mandal,<sup>3,4,5</sup> David Neves,<sup>9</sup> Patrick Mehlen,<sup>9,10</sup> James P. Caruso,<sup>11,12</sup>  Patrick M. Dougherty,<sup>13</sup>  Theodore J. Price,<sup>11</sup> Andrew Chantry,<sup>3,4,5</sup> Michelle A. Lawson,<sup>3,4</sup> Thomas L. Andersen,<sup>2,6,14,15</sup> Juan M. Jimenez-Andrade,<sup>8</sup> and Anne-Marie Heegaard<sup>1</sup>

<sup>1</sup>Department of Drug Design and Pharmacology, University of Copenhagen, Copenhagen 2100, Denmark, <sup>2</sup>Department of Forensic Medicine, Aarhus University, Aarhus 8870, Denmark, <sup>3</sup>Department of Oncology & Metabolism, University of Sheffield, Sheffield S10 2RX, United Kingdom, <sup>4</sup>Mellanby Centre for Bone Research, University of Sheffield, Sheffield S10 2RX, United Kingdom, <sup>5</sup>Sheffield Teaching Hospitals, Sheffield S10 2JF, United Kingdom, <sup>6</sup>The Danish Spatial Imaging Consortium (DanSIC), Denmark, <sup>7</sup>Novo Nordisk Foundation Center for Protein Research, University of Copenhagen, Copenhagen 2200, Denmark, <sup>8</sup>Unidad Académica Multidisciplinaria Reynosa Aztlan, Autonomic University of Tamaulipas, Reynosa 88740, Mexico, <sup>9</sup>NETRIS Pharma, Lyon 69008, France, <sup>10</sup>Apoptosis, Cancer and Development Laboratory-Equipe labellisée 'La Ligue,' LabEx DEVweCAN, Centre de Recherche en Cancérologie de Lyon, Lyon 69008, France, <sup>11</sup>Department of Neuroscience and Center for Advanced Pain, The University of Texas at Dallas, Dallas, Texas 75080, <sup>12</sup>Department of Neurological Surgery, University of Texas Southwestern Medical Center, Dallas, Texas 75390, <sup>13</sup>Department of Pain Medicine, Division of Anesthesiology, MD Anderson Cancer Center, Houston, Texas 77030, <sup>14</sup>Department of Clinical Cell Biology, University of Southern Denmark, Odense 5230, Denmark, and <sup>15</sup>Department of Clinical Pathology, Odense University Hospital, Odense 5000, Denmark

Multiple myeloma (MM) is a neoplasia of B plasma cells that often induces bone pain. However, the mechanisms underlying myeloma-induced bone pain (MIBP) are mostly unknown. Using a syngeneic MM mouse model, we show that periosteal nerve sprouting of calcitonin gene-related peptide (CGRP<sup>+</sup>) and growth associated protein 43 (GAP43<sup>+</sup>) fibers occurs concurrent to the onset of nociception and its blockade provides transient pain relief. MM patient samples also showed increased periosteal innervation. Mechanistically, we investigated MM induced gene expression changes in the dorsal root ganglia (DRG) innervating the MM-bearing bone of male mice and found alterations in pathways associated with cell cycle, immune response and neuronal signaling. The MM transcriptional signature was consistent with metastatic MM infiltration to the DRG, a never-before described feature of the disease that we further demonstrated histologically. In the DRG, MM cells caused loss of vascularization and neuronal injury, which may contribute to late-stage MIBP. Interestingly, the transcriptional signature of a MM patient was consistent with MM cell infiltration to the DRG. Overall, our results suggest that MM induces a plethora of peripheral nervous system alterations that may contribute to the failure of current analgesics and suggest neuroprotective drugs as appropriate strategies to treat early onset MIBP.

**Key words:** cancer-pain; hematology; multiple myeloma; myeloma; pain; sprouting

Received Mar. 7, 2023; revised Apr. 15, 2023; accepted May 12, 2023.

Author contributions: M.D.C., O.P., T.L.A., J.M.J.-A., and A.-M.H. designed research; M.D.C., O.P., T.T.N., D.M.T., N.A.C.-S., J.A.V.-M., L.Y.P.G., H.E., R.E.A., A.M., J.P.C., P.M.D., T.J.P., A.C., and M.A.L. performed research; D.N. and P.M. contributed unpublished reagents/analytic tools; M.D.C., O.P., T.T.N., D.M.T., N.A.C.-S., J.A.V.-M., L.Y.P.G., L.J.J., H.E., D.N., P.M., and J.P.C. analyzed data; M.D.C. wrote the first draft of the paper; M.D.C., O.P., T.T.N., D.M.T., N.A.C.-S., J.A.V.-M., L.Y.P.G., L.J.J., R.E.A., T.J.P., J.M.J.-A., and A.-M.H. edited the paper; M.D.C. wrote the paper.

This work was supported by IMK Almene Fond and Brødrene Hartmanns Fond. Part of this work was supported by the Novo Nordisk Foundation Grant NNF14CC0001. P.M.D. and T.J.P. were supported by the National Institutes of Health (NIH) Grant NS 111929. M.D.-d. and T.L.A. were supported by the

NIH Grant AG 075227. The funding bodies played no role in data collection, analyses, or interpretation, nor in manuscript preparation. We thank Kaja Laursen, Camilla S. Dall, and the animal technicians from the Department of Drug Design and Pharmacology at University of Copenhagen. We also thank the patients for providing their time and agreeing to be part of this project. Figures have been made in BioRender.

The authors declare no competing financial interests.

Correspondence should be addressed to Marta Diaz-delCastillo at [marta@forens.au.dk](mailto:marta@forens.au.dk).

<https://doi.org/10.1523/JNEUROSCI.0404-23.2023>

Copyright © 2023 the authors

### Significance Statement

Multiple myeloma (MM) is a painful bone marrow cancer that significantly impairs the quality of life of the patients. Analgesic therapies for myeloma-induced bone pain (MIBP) are limited and often ineffective, and the mechanisms of MIBP remain unknown. In this manuscript, we describe cancer-induced periosteal nerve sprouting in a mouse model of MIBP, where we also encounter metastasis to the dorsal root ganglia (DRG), a never-before described feature of the disease. Concomitant to myeloma infiltration, the lumbar DRGs presented blood vessel damage and transcriptional alterations, which may mediate MIBP. Explorative studies on human tissue support our preclinical findings. Understanding the mechanisms of MIBP is crucial to develop targeted analgesic with better efficacy and fewer side effects for this patient population.

### Introduction

Multiple myeloma (MM) is an incurable malignant bone marrow disorder characterized by abnormal immunoglobulinemia along with the development of osteolytic bone lesions, hypercalcemia, renal impairment, and anemia (Kyle and Rajkumar, 2009). Research into the mechanisms of MM has grown exponentially over the last few decades, leading to the introduction of novel therapies such as autologous stem cell transplantation, proteasome inhibitors and immunomodulators as first-line treatment for the disease, which altogether have doubled the median survival time of MM patients (Kumar et al., 2008; Kazandjian and Landgren, 2016). As research attempts to convert MM into a chronic condition, improving the patients' quality of life becomes crucial. In a 2016 systematic review of symptom prevalence across MM patients, pain and fatigue were listed as the most common complaints with over 70% of patients reporting pain, which was described as severe in over 40% (Ramsenthaler et al., 2016). Moreover, a profound disconnect exists between the patients' self-reported pain experience and their physicians' estimation, with recent research suggesting that almost half of attending clinicians underestimate the severity of bone pain in this patient population (Quinn et al., 2022).

Today, pain management in MM patients includes disease-modifying agents targeted to reducing bone disease (i.e., bisphosphonates, denosumab, radiotherapy) and opioids, often in combination with a corticosteroid as adjuvant (Niscola et al., 2010; Coluzzi et al., 2019). On top of well-known side effects of opioids, such as constipation, development of tolerance and risk of addiction, their effect on breakthrough pain, a common occurrence in bone cancer, is limited (Mercadante, 2018). Thus, there is an evident need to unravel the pathogenesis of bone pain in MM, which may lead to mechanism-based strategies to alleviate symptom burden and improve quality of life in a growing patient population.

In a previous study, we established a local, immunocompetent mouse model of myeloma-induced bone pain (MIBP) through intrafemoral transplantation of 5TGM1-GFP cells in C57BL/KaLwRijHsd mice (Diaz-delCastillo et al., 2020b). In this model, we observed the development of pain-like behaviors over time, which were only partially reversed by systemic antiresorptive therapy; moreover, our study showed profound bone marrow denervation at the terminal stages of the model. Here, we elucidate central and peripheral dysregulations driving the onset and maintenance of MIBP.

### Materials and Methods

#### Cell culture

Mouse 5TGM1-GFP cells passaged *in vivo* were grown in suspension in RPMI media containing glutamine and phenol red, 1% penicillin/streptomycin (100 U/100 µg/ml), 1% sodium pyruvate (1 mM), 1% MEM

nonessential amino acids, and 10% FBS, at 37°C and 5% CO<sub>2</sub>. All reagents were purchased from Thermo Fischer Scientific.

#### Animals

Male five- to seven-week-old C57BL/KaLwRijHsd mice from Envigo were housed in a temperature-controlled (22 ± 2°C) room with 50% relative humidity under a 12/12 h light/dark cycle (lights on a 7 A.M.). Mice were housed in groups of 4 or 5 in standard individually ventilated GM500<sup>+</sup> cages (524 cm<sup>2</sup>) in a mouse-dedicated room and allowed to acclimatize >7 d before experimental allocation. Cages were enriched with red translucent shelter, an S-brick, paper ropes and corn hidden in the bedding (Tapvei 2HV bedding, Brogaarden). Food (Altromin 1314; Brogaarden) and water were provided *ad libitum*. Experiments were conducted in accordance with the Danish Act on Animal Experiments (LBK No. 474 of 15/05/2014) and approved by the Danish animal Experiments Inspectorate. This manuscript is reported in accordance to the ARRIVE 2.0 guidelines.

#### Experimental design

In a time-course study, mice were intrafemorally inoculated with 5TGM1-GFP myeloma cells or vehicle, their behavior analyzed over time, and euthanized at two different time points (i.e., postsurgical days 17 and 24, respectively) by transcardial perfusion before tissue collection. In the transcriptomics experiment, DRGs from 5TGM1-GFP or vehicle-bearing mice were collected and fresh frozen for further RNA extraction and transcriptome sequencing 24 d after surgery. In the NP137 experiment, mice were dosed with NP137 (10 mg/kg, i.p.) or vehicle biweekly, their behavior analyzed over time and euthanized at end-point by transcardial perfusion before tissue collection. All behavioral testing was conducted in a quiet room during the light phase (between 7 A.M. and 7 P.M.) by the same researcher, who was blinded to experimental group. Mice were randomized according to baseline burrowing capacity or weight. In the time course experiment, mice were randomized into sham or MM according to their baseline burrowing performance and baseline weight. Randomization was performed by listing all mice from lower to higher baseline burrowing capacity or weight and stratifying in two groups. Average baseline burrowing capacity or weight was then calculated and mice were interexchanged among groups until the averages were equal ± 10%. In the transcriptomics experiment, mice were randomized into sham or MM according to weight. To minimize bias and cage, mice from different groups (i.e., MM and sham) were caged together. No physical distinctions among groups were available at mouse or cage level. The allocation code was kept in a close, secure file until the end of the experiment. All behavioral experiments were conducted by an investigator blinded to the experimental group. Exclusion criteria were set to: (1) in all experiments: mice displaying surgical complications, (2) in the time course experiment: 10% worst burrowers (excluded only from burrowing behavior), (3) in the transcriptomics experiment: mice with RNA Integrity Number (RIN) < 8. A total of 16 mice were excluded from data analyses, 14 in the time course experiment (two because of surgical complications, 10 because of cancer contamination in vehicle solution, and two as the 10% worst burrowers), and two in the transcriptomics experiment (RIN < 8.0).

#### Model induction

Mice were anaesthetized with ketamine/xylazine cocktail [85.5 mg/kg ketaminol vet (MSD Animal Health) and 12.5 mg/kg Nerfasin vet

(Virbac, i.p.); eye ointment was applied to prevent dryness (Ophta A/S, Actavis Group). Upon confirmation of loss of pedal reflex, the mouse was placed on a heating pad, the leg was shaved and disinfected with 70% ethanol, and an incision (<1 cm) was made above the right anterior knee. The retinaculum tendon was slightly displaced, and the patella ligament pushed to the side, exposing the distal femoral epiphysis, where hole was drilled with a 30G needle. Through an insulin needle (0.3 ml; BD Rowa Technologies), 10- $\mu$ l of vehicle (Hank Balance Salt Solution, Invitrogen) or cell suspension ( $5 \times 10^4$  5TGM1-GFP cells) were inoculated into the intramedullary femoral cavity. The hole was closed with bone wax (Mediq Danmark A/S), the patella pushed back into place, and the incision closed with surgical clips (Agnthos, Lidingö, Sweden). Mice received 0.5 ml saline (subcutaneous) and two bolus injections of carprofen (5 mg/kg, s.c.; Pfizer), one before surgery and another 24 h after.

#### Limb use

The limb use of freely walking animals was scored as: 4 = normal gait; 3 = insignificant limping; 2 = significant limping and shift in bodyweight distribution toward the healthy limb; 1 = significant limping and motor impairment; 0 = paraplegia, as previously described (Diaz-delCastillo et al., 2020b). Briefly, mice were acclimatized with their cagemates to a standard transparent cage of 125  $\times$  266  $\times$  185 mm for  $\geq$ 10 min. Then, mice were individually transferred to a similar cage where their gait was observed for 3 min.

#### Burrowing

Burrowing capacity was assessed as amount of sand (0–3 mm diameter, ScanSand) displaced from a burrowing apparatus during a 2-h burrowing session (Sliepen et al., 2019). The burrowing apparatus consisted of a gray opaque plastic tube (200  $\times$  72 mm in diameter; frontal end raised 30 mm from the ground) filled with 500 g of sand and placed in a transparent plastic cage (125  $\times$  266  $\times$  185 mm) without bedding, closed with a grid lid. Before baseline measurements, mice were placed in pairs in the cage containing an empty burrowing apparatus for 2 h. On the second and third day, this procedure was repeated but the burrowing tube was filled with 500 g of sand. Throughout the experiment, burrowing was conducted at the same time and in the same room in absence of the researcher.

#### Locomotor activity

Distance and speed moved by freely walking mice was automatically measured with Ethovision XT 8.5 (Noldus Information Technology). On postsurgical day 24, myeloma-bearing and sham mice were individually placed in standard, transparent plastic cages (125  $\times$  266  $\times$  185 mm) in a quiet, dimly illuminated room and their free movement was tracked in 1-min time bins over a total of 15 min.

#### Tissue extraction and analyses

Mice were deeply anaesthetized with a ketamine/xylazine cocktail, as described. Upon loss of pedal reflex, mice were pinned down on their dorsal side and their abdomen and thoracic cage were opened, exposing the beating heart. Transcardial blood was collected with a 27-G needle, before transcardially perfusing with 21–28 ml of ice-cold PBS and 4%PFA-0.12% picric acid (Merck). Spleens were excised and weighed. Ipsilateral femurs were collected, postfixed 24 h in 4% PFA and stored in 70% ethanol until  $\mu$ CT analyses were performed, and in 0.1 M PBS afterward. Spinal cords and lumbar DRGs were postfixed 24 h in 4% PFA-0.12% picric acid, dehydrated in 30% sucrose and embedded in OCT. In the transcriptomics experiment, mice were perfused with 10 ml of ice-cold PBS and their lumbar DRGs quickly extracted and fresh-frozen in RNase-free Eppendorf tubes in a 3-methylbutanol freezing bath.

#### Serum IgG2b analyses

Blood was left undisturbed at RT for 30–90 min and thereafter centrifuged 10 min at 4°C and 6000 RPM. Serum was stored at –80°C and IgG<sub>2b</sub> was measured with a sandwich ELISA kit (Bethyl Laboratories, #E99-109; AB\_2892024) following manufacturer's recommendations.

#### $\mu$ CT analyses

Ipsilateral femurs were analyzed in a SkyScan 1272 *ex vivo* scanner at 50 kV and 200 mA, as previously described (Lawson et al., 2015). A 0.5-mm aluminum filter and a pixel size of 4,3 mm<sup>2</sup> were used. Following standard guidelines (Bouxein et al., 2010), the following morphometric parameters were assessed: bone volume per total volume (BV/TV), bone surface per bone volume (BS/BV), bone surface per total volume (BS/TV), trabecular thickness (Tb.Th), trabecular spacing (Tb.Sp), trabecular number (Tb.N), and lesion area. Representative 3D models were re-created with ParaViewSoftware. For the anti-netrin experiments, scans were reconstructed using NRecon software (version 1.6.1.1; SkyScan) within a dynamic range of 0–0.15 and a ring artifact reduction factor of 5%. Reconstructed images were analyzed using CTAN (version 1.9.1.1 Bruker). Analysis was done on the cross-sectional images of the tibias or femurs at 1.2 mm (offset) from the distal break in the growth plate (reference point), on a fixed 1-mm region. The trabecular bone was carefully traced on all cross-sectional images of the distal femur and BV/TV was calculated.

#### Immunohistochemistry in lumbar DRGs

Lumbar DRGs were serially sectioned at 16- $\mu$ m thickness. Slides were washed thrice, permeabilized in 0.1% Triton X-100/T-PBS and blocked with 1% BSA or 3% NDS before antibody labeling against activating transcription factor 3 (ATF3; either 1:200 polyclonal, rabbit anti-mouse, Novusbio; #NBP1-85 816, AB\_11014863, or 1:400 polyclonal, rabbit anti-mouse, Santa Cruz; #SC-188, AB\_2258513), tyrosine hydroxylase (TH), a marker for postganglionic sympathetic neurons (TH polyclonal rabbit anti-mouse; 1:1000, Millipore; #AB152, AB\_390204), CD31, a marker of blood vessel endothelial cells (CD31 monoclonal rat anti-mouse, 1:500, BD Pharmingen; #557355, AB\_396660), or GFP (GFP polyclonal chicken anti-mouse; 1:2000, Invitrogen; #A10262, AB\_2534023). After, slides were washed and incubated 3 h with secondary antibodies: Alexa Fluor 488 (anti-rabbit, 1:1000, Invitrogen, Thermo Fisher Scientific, #A11008, AB\_143165), Cy3 (monoclonal donkey anti-rabbit 1:600; Jackson ImmunoResearch; #711-165-152, AB\_2307443), Cy2 (polyclonal donkey anti-chicken, 1:400; #703-225-155, AB\_2340370). Sections were counterstained with DAPI (1:10,000, Sigma-Aldrich; #D21490) for 5 min, dehydrated in an alcohol gradient and rinsed in xylene. Slides were mounted DPX or fluorescent mounting medium containing DAPI (DAKO Agilent).

#### DRG neuronal profile quantifications

Serial DRG sections were separated by >120  $\mu$ m to prevent duplicate counting of neuronal cell bodies. At least a confocal image from three different sections under a 20 $\times$  objective per animal was taken on a Zeiss LSM 800 confocal microscope. The number of ATF3<sup>+</sup> or TH<sup>+</sup> immunoreactive neuronal profiles in sensory ganglia were determined in ImageJ (NIH), as previously reported (Peters et al., 2005), by quantifying both labeled and nonlabeled neuronal profiles.

#### DRG blood vessel quantifications

Quantification was performed by counting the number of CD31<sup>+</sup> blood vessels per unit volume (area  $\times$  thickness; Ireland et al., 1981; Glaser et al., 2004; Jimenez-Andrade et al., 2008), where blood vessels were identified as CD31<sup>+</sup> and 2–10  $\mu$ m in diameter; CD31<sup>+</sup> branched blood vessels were counted as one single vessel (Weidner et al., 1991). DRG sections were initially scanned at low magnification (10 $\times$ ) to identify the areas with the highest density of CD31<sup>+</sup> blood vessels and then a confocal image was obtained at 40 $\times$  magnification. At least three pictures per animal were taken. An extended depth of focus processing was performed on all Z-stack files for each image and total number and length of CD31<sup>+</sup> blood vessels within cell body-rich areas (Hirakawa et al., 2004) were determined using ImageJ (NIH). Then this area was multiplied by the thickness of the section (16  $\mu$ m).

#### Immunohistochemistry in spinal cords

Spinal cords were serially sectioned at 30- $\mu$ m thickness; lumbar regions L1 to L6 were identified as per their described gray matter anatomy (Watson et al., 2009) and collected. Slides were washed in PBS, permeabilized in 0,1% Triton X-100 in PBS and blocked with 2% BSA (Sigma-

Aldrich). Then, slides were o/n incubated with a rabbit antibody against Iba-1 (Wako Pure Chemical Industries, Ltd.), GFAP (DAKO Agilent), or P-p38 (Thr180/Tyr182; Bionordika, Cell Signaling Technology) at 4°C. Labeling was detected with an Alexa Fluor 594 goat anti-rabbit secondary antibody or Alexa Fluor 594 donkey anti-rabbit (1:300, Invitrogen, Thermo Fisher Scientific). Slides were then washed, counterstained with DAPI (Thermo Fisher Scientific) and mounted with Fluorescent Mounting Medium (DAKO Agilent). Negative controls were performed by omission of primary antibody. Serial sections separated by at least 240  $\mu\text{m}$  were imaged with a 20 $\times$  objective using a Zeiss Axioskop 2 microscope with a high resolution AxioCam MRm camera (HAL100; Zeiss) and a fluorescent transmitter (HXP 120, Digital Scientific). Pseudo-anonymized images were analyzed in ImageJ (National Institutes of Health) by a researcher blinded to experimental mouse and group. Briefly, positive Iba-1 and P-p38 cells were quantified within a predetermined area of interest (347  $\times$  260  $\mu\text{m}^2$ ) located in the dorsal horn and including Laminae I–IV. GFAP was quantified by measuring fluorescence intensity in the dorsal horn and calculating the corrected total cell fluorescence (CTCF) as previously described by us and others (Ansari et al., 2013; Diaz-delCastillo et al., 2018).

#### Immunohistochemistry in femurs

Following  $\mu\text{CT}$ , femurs were decalcified in 10% EDTA for two weeks at 4°C before cryoprotection in 30% sucrose and 4°C storage; decalcification was monitored using a portable x-ray equipment (Fona X70, Fona). Femurs were longitudinally cut in a frontal plane (25- $\mu\text{m}$  thickness) with a cryostat (Leica 1900, Leica Biosystems), mounted on slides (Superfrostplus, Thermo Scientific; #J1800AMNZ) and allowed to dry (30 min, RT). Subsequently, slides were placed in vertical chambers (Shandon, Sequenza Immunostaining, Fisher Scientific; #73-310-017), washed, blocked (3% normal donkey serum, 0.3% Triton X-100 in PBS) for 2 h RT and incubated o/n with a primary antibody cocktail containing anti-GFP antibody (polyclonal chicken anti-GFP, 1:2000; #A10262, AB\_2534023; Thermo Fisher Scientific), anti-TH antibody (TH polyclonal rabbit anti-mouse; 1:1000, Millipore; #AB152, AB\_390204), and an antibody against calcitonin gene-related peptide (CGRP; polyclonal rabbit anti-rat, 1:5000; #C8198, AB\_259091; Sigma-Aldrich), or growth associated protein-43 (GAP43; rabbit anti-GAP43; 1:1000; #AB5220, AB\_2107282; Millipore). Subsequently, sections were washed and then incubated 3 h with a secondary antibodies cocktail of Cy3 donkey anti-rabbit (1:600; Jackson ImmunoResearch; #711-165-152, AB\_2307443) and Cy2 donkey anti-chicken (1:400; Jackson ImmunoResearch; #703-225-155, AB\_2340370). Slides were counterstained with DAPI for 5 min (1:20,000, Sigma-Aldrich; #D21490), washed, dehydrated through an alcohol gradient and xylene, and sealed with DPX mounting medium (slide mounting medium; Sigma-Aldrich; #06522).

#### Quantification of the density of nerve fibers on femoral periosteum and neuroma identification

For quantifications of CGRP<sup>+</sup> and GAP43<sup>+</sup> nerve fibers density, at least three sections of each mouse femur were analyzed by the same researcher, blinded to model allocation and treatment group. The areas with the highest density of nerve fibers at the metaphyseal periosteum were identified using a 10 $\times$  objective. In all cases, these areas were located within 0.5- to 1-mm distance from the distal femoral growth plate. Subsequently, a confocal image was obtained using the Z-stack function from a Carl Zeiss confocal microscope (model LSM 800). At least three images were obtained for each marker (20 $\times$  magnification). The Z-stacked images were analyzed with ImageJ and nerve fibers were manually traced to determine their total length using the freehand line tool. Area of evaluation was manually determined tracing the area of the periosteum. This area was multiplied by the thickness of the section (25  $\mu\text{m}$ ). Results were reported as the density of nerve fibers (total length) per volume of periosteum ( $\text{mm}^3$ ; Mantyh et al., 2010).

For the identification of neuroma-like structures, the following three criteria was followed (1) disordered mass of blind-ending axons (CGRP<sup>+</sup>) that had an interlacing and/or whirling morphology, (2)

structure with a size of >10 individual axons that is at least 20  $\mu\text{m}$  thick and 70  $\mu\text{m}$  long, and finally (3) a structure that is never observed in the periosteum of normal bone (Devor and Wall, 1976; Sung and Mastro, 1983).

#### Evaluation of human bone

Trephine iliac crest bone biopsies from newly diagnosed MM (NDMM) patients were collected at Sheffield Teaching Hospital on informed consent and under approval from the East Midlands-Derby Research Ethics Committee, United Kingdom (REC19/YH/0319). Needle (3 mm) biopsies were collected under local lidocaine anesthesia by a qualified medical practitioner as routine standard of care. Biopsies were formalin-fixed o/n, decalcified in formic acid, and paraffin embedded before sectioning at 3.5- $\mu\text{m}$  thickness onto DAKO IHC Flex tissue slides (DAKO Aps). Sections were deparaffinized in a xylene and alcohol gradient and subjected to antigen retrieval in Tris-EDTA buffer (pH 9.0) o/n. Slides were washed, blocked for endogenous peroxidases and blocked for unspecific staining 20 min in 5% casein/TBS. Sections were labeled with a rabbit anti-PGP9.5 antibody (Sigma-Aldrich; #SAB4503057, AB\_10761291), detected with polymeric alkaline phosphatase conjugated anti-rabbit IgG (BrightVision DPVR-AP, Immunologic) and visualized with stay red (DAKO). Next, sections were labeled with a mouse mAb against CD34 (Abcam; #ab78165, AB\_1566006), detected by polymeric horse radish peroxidase conjugated anti-mouse IgG (BrightVision DPVR-HRP, Immunologic) and visualized with deep space black (DSB, CCC). Sectioned were then blocked with mouse serum and labeled with a mouse mAb against CD138 (BD Pharmingen; #552723, AB\_394443), which was detected with horse radish peroxidase conjugated anti-fluorescein Fab fragments (Merck) and visualized with diaminobenzidine (DAB<sup>+</sup>; DAKO). Finally, sections were counterstained with Mayer's hematoxylin and mounted in Aquatex (Merck). Slides were brightfield scanned with a 20 $\times$  objective in an automated VS200 Slidescanner (Olympus Microscopy) and analyzed in VS200 Desktop (Olympus) by an experimenter blinded to the slide origin.

#### Mouse transcriptomics sequencing and analyses

In the transcriptomics experiment, 20 male C57BL/KaLwRijHsd mice underwent inoculation of 5TGM1-GFP cells or vehicle as described. Pain-like behaviors were assessed over time and mice were euthanized 24 d after surgery by transcardial perfusion with 10 ml of ice-cold PBS. Serum samples were collected and processed for IgG<sub>2b</sub> assessment as described. Ipsilateral whole DRG lumbar L2-L4 were snap frozen in RNase free Eppendorf tubes in a 3-methylbutanol freezing bath. Tissue was homogenized in a bead miller and total RNA was extracted with a Qiagen RNase microkit (QIAGEN). RNA quality was assessed with an Agilent Bioanalyzer and samples with a RIN <8.0 were excluded ( $n = 2$ ).

Remaining samples underwent DNBSEQ transcriptome sequencing by BGI Denmark (BGI). Fastq files with reads with adaptors removed were further used in the bioinformatics analysis on filtering out low quality ends. We used Salmon (version 1.5.2; Patro et al., 2017) to quantify transcript expression, using as reference the mouse cDNA set (coding and noncoding transcripts) corresponding to GRCh39. The salmon index was built using the corresponding GRCh39 genome as decoy sequence. Both the cDNA set and genome were obtained from Ensembl, release 104 (Howe et al., 2021; Cunningham et al., 2022). Gene-level expression estimates were further obtained using the tximport R package (Soneson et al., 2015). Genes with non-zero counts in at least three samples and with at least 10 estimated mapped reads in at least one of the samples were retained for further analysis. Differential expression analysis between the MM and sham was performed using the Wald test from DESeq2 R package (Love et al., 2014).

Metastatic infiltration of MM cells within the DRG was assessed from the sequencing reads by counting the reads mapping to the eGFP, an artificial transfect to the 5TGM1 cell line. Bbduk (bbmap suite, v. 38.90; Bushnell, 2021) with a kmer size of 31 was used to find the proportion of eGFP matching reads in each sample; eGFP sequences retrieved from (SnapGene, Dotmatics; <https://www.dotmatics.com/solutions/snapgene>).

GSEA (gene set enrichment analysis) for GO biological processes terms and reactome pathways was performed using the R packages clusterProfiler (Sacks et al., 2018) and ReactomePA (Yu and He, 2016). Genes were ranked using the Wald test statistic (stat value) provided by DESeq2. We used the pairwise\_termsim() function from enrichplot (Yu, 2019) to obtain the Jaccard similarity coefficient (JC) in terms of overlapping gene sets between each two terms. Whenever JC was >0.7, we selected only the term with lowest adjusted *p*-value value in our enrichment results. Visualizations of the enrichment results were produced using the R packages DOSE (Yu et al., 2015) and enrichplot (Yu, 2019), and data are accessible in Gene Expression Omnibus (GEO) under accession code GSE216802.

We compared our MM mouse data with DRG expression data from 6 other mouse models of painful conditions, as described previously (Bangash et al., 2018). The transcriptomes of DRGs from the test mice and their corresponding sham had been profiled using the Affymetrix GeneChip Mouse Transcriptome Array 1.0 and obtained from Additional file 3 (Bangash et al., 2018). We compared our model with the six models in terms of overlap and direction of differentially expressed genes (DEGs), as well as in terms of GSEA results. For our MM model we used the set of DEGs defined as *padj* < 0.05, and for the models from Bangash et al., we used the sets of top 300 genes, sorted by *p*value. GSEA analysis for the six models was performed as described for our MM transcriptomic data but ranking the genes by  $-\log(\text{pvalue}) \times (\log\text{FC}/\text{abs}(\log\text{FC}))$ . For comparing GSEA results, we selected top 40 most enriched terms in the mouse MM model, sorted by absolute normalized enrichment score, and then extracted the values of the respective terms within the enrichment results corresponding to the other models.

#### Human transcriptomics sequencing and analyses

Human DRGs were collected from consenting cancer patients under ethical approval from UT Dallas (UTD) and MD Anderson Cancer Centre Institutional Review Boards. Tissue was extracted during thoracic vertebrectomy in patients presenting malignant spinal tumors; sequencing data from these patients has been previously published by Ray and colleagues, where the demographic and clinical characteristics of the cohort are described (Ray et al., 2023). Briefly, DRGs were extracted during spinal nerve root ligation and immediately transferred to cold sterile solution, cleaned and stored in dry ice until sequencing. RNA was extracted using TRIzol and cDNA was generated using an Illumina TruSeq library preparation. Sequenced reads were then trimmed and same-length libraries (38 bp) mapped to the GENCODE reference transcriptome (Frankish et al., 2019), as previously described (Ray et al., 2023). Data were obtained from two DRGs belonging to one MM patient and 68 DRGs obtained from 39 patients; further information is compiled in Extended Data Figure 9-1. To evaluate gene expression profiles consistent with MM cell infiltration to the DRG, we first created a custom-made marker set from publicly available data. For this, we combined three high throughput datasets of MM cell gene expression based on different technologies: Affymetrix (Barwick et al., 2021), bulk RNA-Seq (Zhan et al., 2006), and single-cell RNA-Seq (Jang et al., 2019), and one dataset measuring expression in normal human DRGs (Ray et al., 2018). For the Affymetrix (Barwick et al., 2021) dataset, we obtained the processed data from the GEO NCBI portal using the GeoQuery R package (v.2.60.0; Davis and Meltzer, 2007). We mapped the probesets of the HGU133Plus2 chip to Ensembl genes using the custom annotation provided by BrainArray (Dai et al., 2005). The file mapping probesets to Ensembl genes was obtained from the BrainArray download page, version 25 (<http://brainarray.mbni.med.umich.edu>). Probesets mapping to multiple genes were excluded and when multiple probesets corresponded to the same gene, the one with the highest mean average signal was selected. Probeset intensities were averaged across the 559 replicates, and in total, 16,554 Ensembl genes (of which 15,994 having the biotype “protein coding genes”) were uniquely mapped to probesets on the chip. We assigned ranks to genes by sorting them by decreasing average signal intensity. For the RNA-Seq dataset (Zhan et al., 2006), we used the supplementary table with FPKM counts provided in the Gene Expression Omnibus (GEO) platform (study accession number GSE167968). We averaged expression levels across the 33 replicates and ranked genes by decreasing average

FPKM units. For the single cell dataset (Jang et al., 2019), we used the supplementary file with transcripts per million (TPM) counts provided in GEO (GSE118900), and counted the number of cells (out of a total 597) in which each gene has a non-zero expression level. Normal DRG expression levels (Ray et al., 2018) were ranked by the decreasing average TPM counts across the three normal tissue samples. Combining the three MM transcriptomic datasets, we obtained a set of 2528 genes generally expressed in MM cells, i.e., ranked within the top 10,000 genes in both Affymetrix and bulk RNA-Seq and detected in at least 200 of the 597 cells of the single cell experiment. We further reduced this set to a subset of 40 genes by selecting those with an expression rank >15,000 (corresponding to <0.75 TPM) in normal DRG tissue.

We next interrogated MM cell infiltration in human DRG using the MM<sup>D24</sup> mouse transcriptomic signature as a proxy. For this, we selected the set of upregulated DEGs with a *p*-adjusted < 0.05 in MM<sup>D24</sup> versus sham<sup>D24</sup> mice and evaluated the behavior of their human orthologs in the DRG of MM patients compared with DRGs from patients with other cancer types. For each of the selected markers/DEGs, and for each cancer sample, we computed the percentile expression in relation to the other cancer samples.

#### Experimental design and statistical analysis

With exception of the transcriptomics experiments (see Human transcriptomics sequencing and analyses), data were analyzed and plotted using GraphPad Prism v.9.3.1 (GraphPad Inc.), or SAS 9.4 (SAS Institute) and are presented as mean ± SEM. Group size was determined in G\*Power v3.1.9.7 based on our previously published data (Diaz-delCastillo et al., 2020b) to detect a significant difference in limb use on postsurgical day 25 with a 90% power ( $\alpha$  error prob. 0.05). Parametric data were analyzed by Student's *t* test, one-way ANOVA or repeated measures two-way ANOVA with Tukey's correction for multiple comparisons, as required. Nonparametric data were analyzed by Friedman's two-way test followed by Wilcoxon's two-sample test for individual time points. Transcriptomics data are available in Extended Data Figure 6-1 or publicly available in GEO (GSE216802); all other data are available on request.

## Results

### Intrafemoral inoculation of 5TGM1-GFP cells induces pain-like behaviors

To understand the time course of neuronal changes leading to MIBP and the mechanisms involved, we conducted a time course study where C57BL/KaLwRijHsd mice were transplanted with 5TGM1-GFP MM cells or vehicle into the medullary cavity of the femur and their pain-like behaviors were assayed over time (Fig. 1A). A subset of animals was then euthanized on postsurgical day 17 (sham<sup>D17</sup> and MM<sup>D17</sup>), before development of pain-like behaviors (Fig. 1B,C) and another on postsurgical day 24 (sham<sup>D24</sup> and MM<sup>D24</sup>), on the onset of nociception, as measured by the limb use and burrowing tests (Fig. 1D,E). The choice of nonstimulus evoked behavioral test was informed by our previous model characterization, where we have demonstrated that this model is not sensitive to mechanical or heat hyperalgesia (Diaz-delCastillo et al., 2020b). Locomotor activity test was performed to ensure that the observed behavioral deficits were not a result of impaired motor function (Fig. 2). Disease development was confirmed by paraproteinemia in both animal cohorts (Fig. 1G,J). MM<sup>D24</sup> mice, but not MM<sup>D17</sup> mice, also presented splenomegaly (Fig. 1F,H), a common feature of 5T MM animal models.

### 5TGM1-GFP cells induce a time-dependent pattern of osteolytic lesion development

In previous experiments we observed a partial analgesic effect of bisphosphonates in the localized 5TGM1 model (Diaz-delCastillo et al., 2020b), suggesting that MIBP may correlate with osteolysis. Similarly, a plethora of clinical studies have shown that, like in

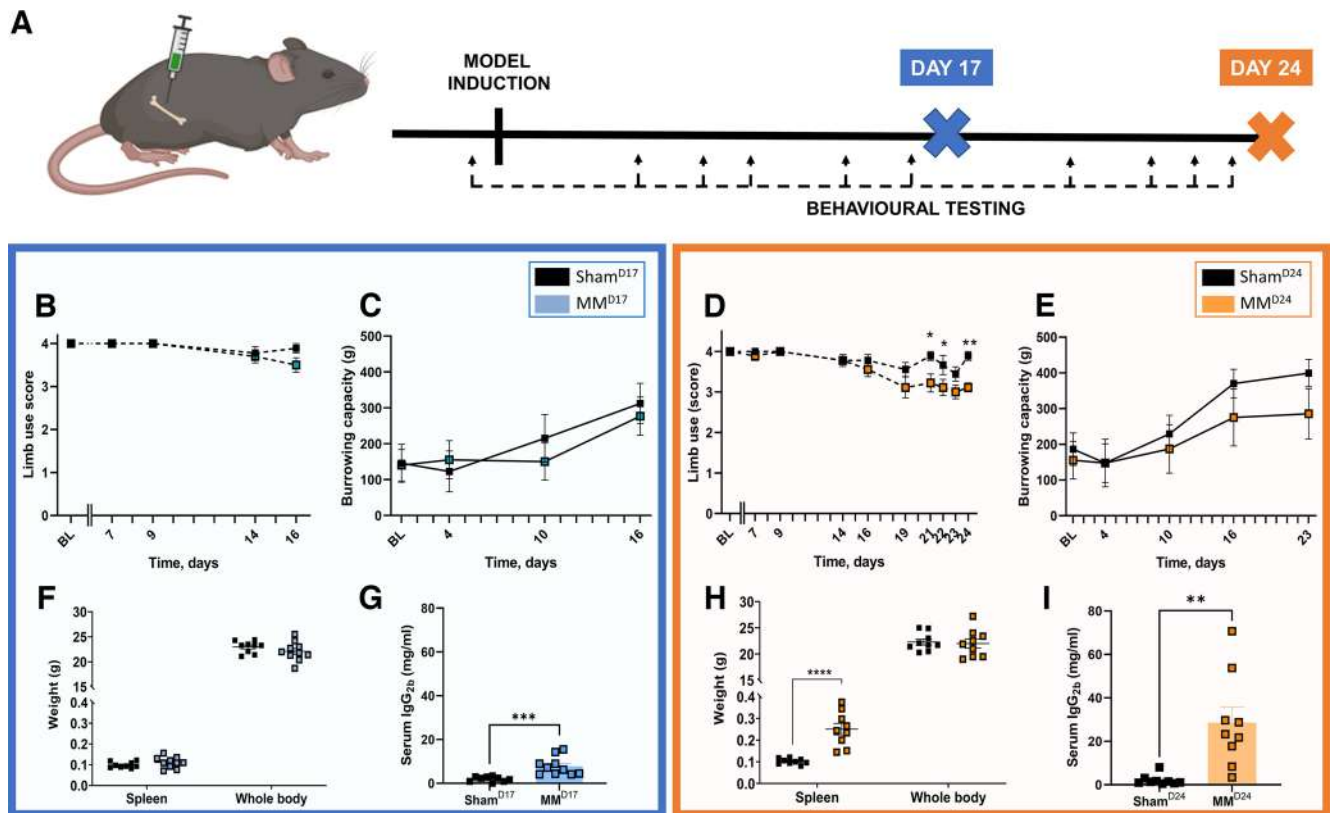


**Figure 1.** Intrafemoral 5TGM1-GFP cell inoculation in C57BL/KaLwRijHsd mice induces MM disease and pain-like behaviors over time. **A**, C57BL/KaLwRijHsd mice were intrafemorally inoculated with 5TGM1-GFP cells or vehicle, their pain-like behaviors were assessed over time, and mice were euthanized on postsurgical day 17 or 24. **B, D**, Limb use scores were measured over time.  $F_{(1,180)} = 2.10$ ,  $p = 0.0226$ . D21:  $p = 0.0167$ ; D22:  $p = 0.0369$ ; D24:  $p = 0.0029$  by Friedman's two-way test followed by Wilcoxon's two-sample test. **C, E**, Burrowing capacity was assessed over time. **F, H**, End-point spleen and whole-body weight.  $t_{(14)} = 5.98$ ,  $p < 0.0001$  by unpaired, two-tailed Student's *t* test. **G, I**, Endpoint serum levels of IgG<sub>2b</sub> paraprotein. D17:  $t_{(17)} = 4.068$ ,  $p = 0.0008$ ; D24:  $t_{(16)} = 3.70$ ,  $p = 0.0019$  by unpaired, two-tailed Student's *t* test. BL = baseline; D = day. Sham  $n = 8$ –9; MM  $n = 8$ –10.

animal models, the clinical analgesic effect of bisphosphonates in MIBP is unclear (Mhaskar et al., 2017). To examine whether the pattern of myeloma-induced osteolysis correlates with the onset of nociception in this model, we performed  $\mu$ CT analyses of the ipsilateral femoral metaphysis of sham and myeloma-bearing bones. We observed that MM<sup>D24</sup> present a significant increase in cortical lesion area/bone surface (BS), compared with sham<sup>D24</sup> (Fig. 3I,J). In contrast, the lesion area/BS of MM<sup>D17</sup> remained unchanged, indicating that osteolytic cortical damage develops concurrently to the onset of nociception (Fig. 3A,B). Furthermore, our analyses revealed unchanged cortical bone volume in both MM<sup>D17</sup> and MM<sup>D24</sup> femurs (Fig. 3C,K).

Next, we evaluated the effect of 5TGM1 cell inoculation in trabecular bone before and during nociception. Densitometric analyses of MM<sup>D17</sup> trabecular bone revealed a significant decrease in trabecular thickness (Tb.Th) and number (Tb.N), along with increased trabecular spacing (Tb.S), indicating trabecular bone loss before the development of nociception (Fig. 3F–H). Moreover, MM<sup>D17</sup> femurs presented decreased trabecular bone volume per total volume (BV/TV) and increased relative bone surface (BS/BV), compared with sham<sup>D17</sup> (Fig. 3D, E). As expected, MM<sup>D24</sup> femurs presented a similar pattern of trabecular osteolysis, measured as significantly decreased BV/TV and Tb.N., along with increased Tb.Sp (Fig. 3L–P).

#### Multiple myeloma induces periosteal nerve sprouting concomitant to nociception

Our previous studies revealed that 5TGM1 inoculation induced complete bone marrow denervation at the end stages of the

model, leading us to speculate that tumor-induced nerve injury contributes to MIBP. To further evaluate the temporal effect of 5TGM1 cell inoculation on the bone marrow microenvironment, we performed immunohistological analyses of sensory (calcitonin-gene related peptide, CGRP<sup>+</sup>) and sympathetic (tyrosine hydroxylase, TH<sup>+</sup>) nerve fibers. We observed that already in MM<sup>D17</sup> femurs, TH<sup>+</sup> and CGRP<sup>+</sup> fibers were not detectable in the bone marrow, which had been colonized by 5TGM1-GFP<sup>+</sup> cells (Fig. 4E,G), suggesting that tumor-induced nerve injury precedes the development of MIBP. To confirm that the absence of marrow innervation was not a result of technical difficulties, we identified both TH<sup>+</sup> and CGRP<sup>+</sup> nerve fibers in bones of the sham<sup>D17</sup> mice (Fig. 4B–D) and in the periosteum of sham<sup>D17</sup> (Fig. 4A,C) and MM<sup>D17</sup> (Fig. 4F,H).

We next sought to examine the effect of intrafemoral 5TGM1-GFP inoculation on periosteal innervation. The periosteum is the bone compartment with the highest nerve density (Mach et al., 2002; Chartier et al., 2018) and alterations to periosteal nerve fiber innervation have been described as a feature of bone pain (Martin et al., 2007; Mantyh, 2014), including cancer-induced bone pain (Mantyh et al., 2010; Bloom et al., 2011). Our analyses revealed infiltration of MM cells to the femoral periosteum of MM<sup>D24</sup>, which were not present in MM<sup>D17</sup> femurs. Importantly, we found a significant increase in the density of CGRP<sup>+</sup> fibers innervating the periosteum of MM<sup>D24</sup> mice at the onset of nociception, compared with sham<sup>D24</sup> (Fig. 4I,M,O), which was not present at earlier stages (Fig. 4K,O). Similarly, the growth associated protein-43 (GAP-43) marker of axonal growth and regeneration demonstrated significant periosteal sprouting in the later stage of MM

development (Fig. 4J,L,N,P). Altogether, our data suggests that MM cells induce cortical osteolytic lesions that allow escape to the periosteum, where they may promote periosteal nerve sprouting and contribute to the development of nociception. This was further supported by the significant inverse correlation between periosteal CGRP<sup>+</sup> and GAP43<sup>+</sup> periosteal nerve sprouting and burrowing capacity (Fig. 4Q,R).

To investigate the human relevance of our findings, we next performed an explorative study to evaluate whether periosteal infiltration of MM cells in patients is associated with nerve sprouting. In formalin-fixed, paraffin-embedded trephine iliac crest bone biopsies from 13 newly diagnosed MM (NDMM) patients, we performed a multiplex immunostaining for CD138<sup>+</sup> MM cells, CD34<sup>+</sup> blood vessels and the pan-neuronal marker PGP9.5 (Fig. 4S). Our quantification showed that the median periosteal nerve density in NDMM patients was 3.736 profiles/mm<sup>2</sup>, ranging from 0 to 82.869 profiles/mm<sup>2</sup> (Fig. 4T); this is in contrast with reports of periosteal nerve density in noncancerous patients showing a median of 0.077 profiles/mm<sup>2</sup> (range: 0.02–0.68 profiles/mm<sup>2</sup>; Sayilekshmy et al., 2019). Moreover, we found a significant increase in periosteal nerve density in NDMM displaying periosteal infiltration of CD138<sup>+</sup> cells compared with patients without CD138<sup>+</sup> cells in the periosteum (Fig. 4U), suggesting a direct role for MM cells in promoting nerve sprouting. Periosteal nerve density in NDMM patients was positively correlated with age (Fig. 4V) but independent of tumor burden, which was assessed as percentage bone marrow clonality (Fig. 4W) and paraproteinemia (Fig. 4X). Moreover, periosteal nerve density was independent of sex and IgG type (data not shown). This is, to our knowledge, the first evidence of MM-induced alterations to bone innervation in MM patients and altogether our data suggest that periosteal nerve sprouting may play a role in MIBP.

### Pharmacological blockade of periosteal nerve sprouting induces a transient anti-nociceptive effect

Next, we tested the mechanistic role of periosteal nerve sprouting on MIBP using a therapeutic anti-netrin-1 blocking antibody (NP137). Netrin-1 is an axon guidance molecule known to play a pivotal role in neurogenesis through binding to its canonical receptors UNC5 homolog (UNC5H) and deleted in colorectal cancer (DCC; Madison et al., 2000; Dun and Parkinson, 2017; Boyer and Gupton, 2018). Previous studies have demonstrated a role of netrin-1 on sensory nerve sprouting (Zhu et al., 2019); moreover, silencing netrin-1 reduces hyperalgesia and CGRP<sup>+</sup> nerve fiber sprouting in a rat model of disk degeneration (Zheng et al., 2023) and pharmacological netrin-1 inhibition with the NP-137 anti-netrin-1 antibody reduced hyperalgesia in an arthritis model (Rudjito et al., 2021). To investigate whether blockade of periosteal nerve sprouting attenuated MIBP, 5TGM1-GFP inoculated mice were systemically treated with vehicle (MM<sup>VEH</sup>) or

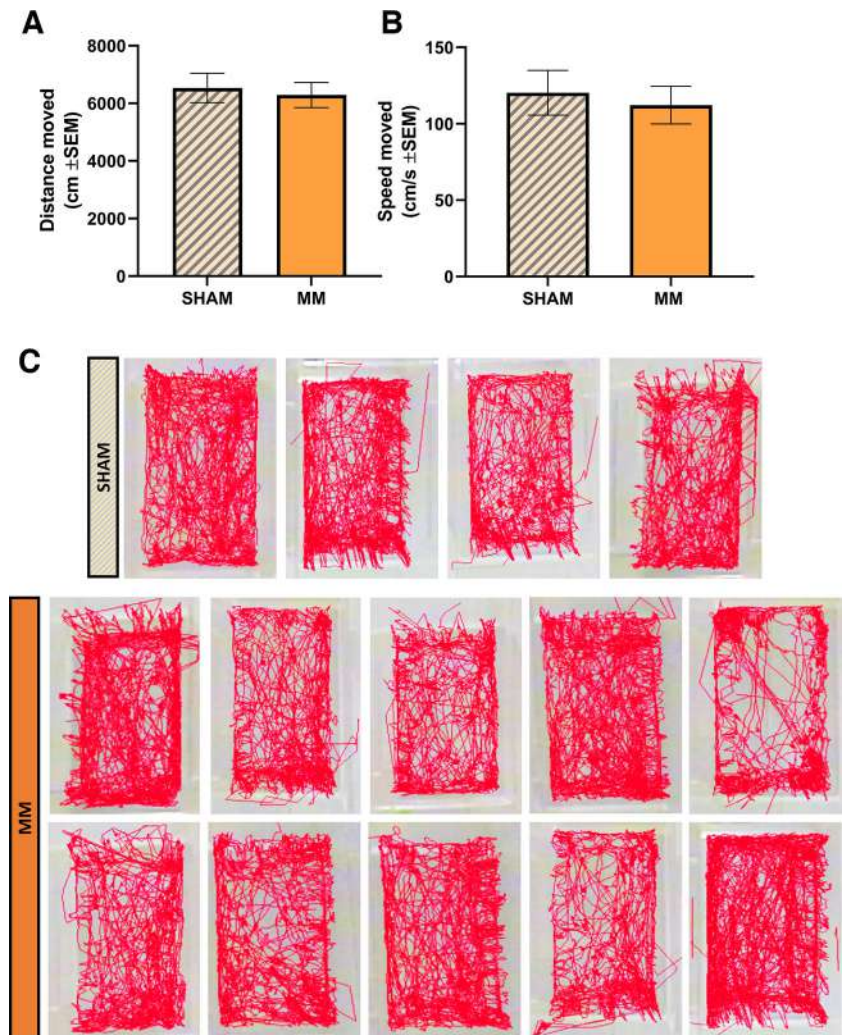


**Figure 2.** The mobility of myeloma-bearing mice was unaffected by disease progression. On postsurgical day 24, distance moved (A) and speed moved (B) on MM mice and sham were not significantly different, indicating that the MIBP deficits in the limb use score are not caused by motor impairment. C, Trajectory plot of each individual sham and MM mouse. Data are analyzed by two-tailed unpaired Student's *t* test and presented as mean ± SEM. Sham *n* = 4; MM *n* = 10.

NP137 (MM<sup>NP137</sup>; 10 mg/kg, i.p). Biweekly treatment with the anti-netrin-1 antibody did not have an overall behavioral effect, but it delayed the onset of pain-like behavior, inducing a significant improvement in limb use scores in MM<sup>NP137</sup> on day 26, compared with MM<sup>VEH</sup> (Fig. 5A). Moreover, NP137 treatment did not affect overall survival (Fig. 5B) nor overall tumor burden, as assessed by terminal splenomegaly (Fig. 5C). To evaluate whether the transient analgesic effect was a consequence of decreased osteolysis, we performed  $\mu$ CT analyses of endpoint MM<sup>VEH</sup> and MM<sup>NP137</sup> femurs. Our results demonstrated that netrin-1 blockage does not affect BV/TV in MM mice (Fig. 5D). Moreover, the structural parameters of trabecular bone and bone mineral density were unchanged (data not shown). To confirm the capacity of NP137 treatment to block periosteal nerve sprouting, we next assessed the presence of CGRP<sup>+</sup> nerve fibers in the femoral periosteum and found a significant reduction in CGRP<sup>+</sup> periosteal nerve density in MM<sup>NP137</sup>, compared with MM<sup>VEH</sup> (Fig. 5F–H). Anatomical presence of a microneuroma was observed in 25% of the vehicle-treated MM mice (Fig. 5H), a feature of the disease never before described but that is consistent with animal models of solid bone cancers such as prostate (Jimenez-Andrade et al.,

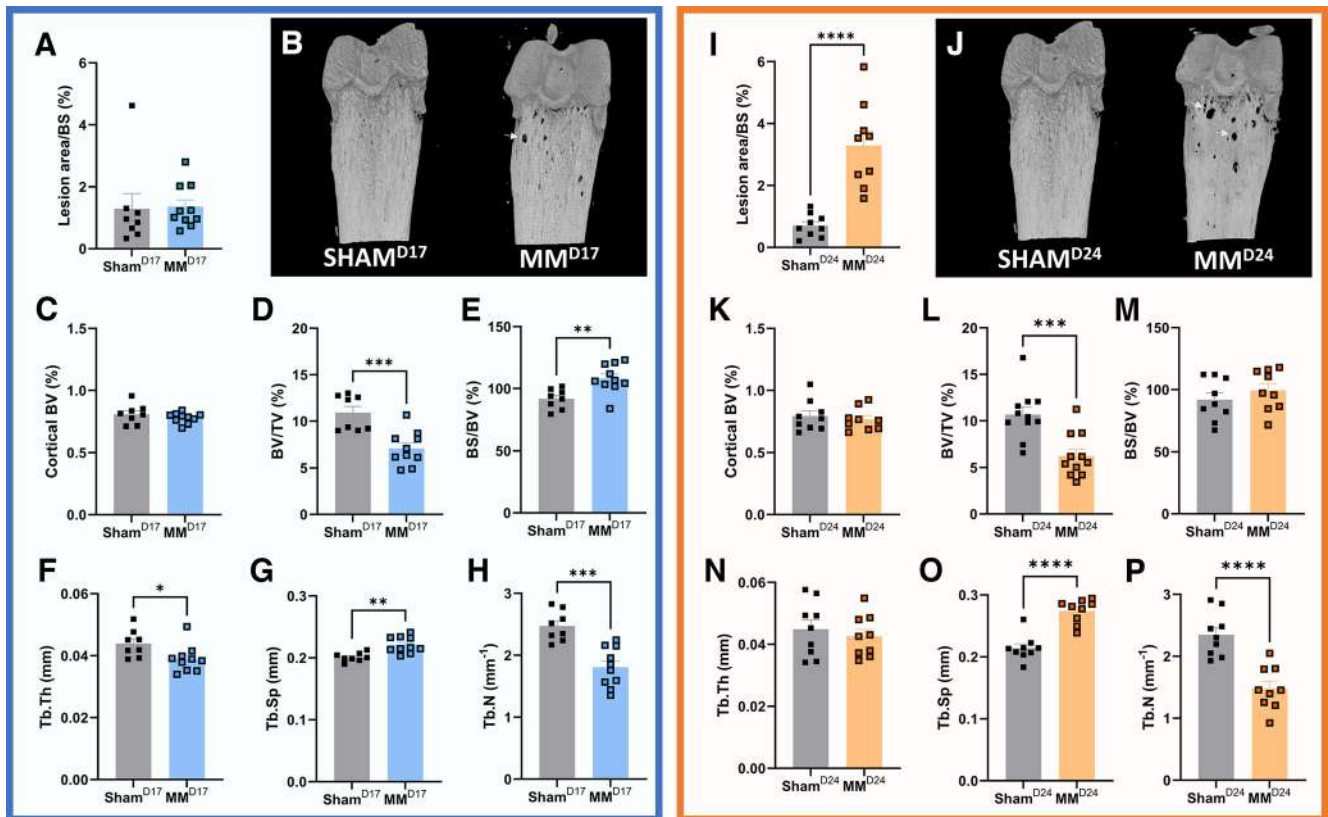


**Figure 3.** Temporal evolution of myeloma-induced bone disease in 5TGM1-GFP bearing femurs. **A, I**, Percentage of lesion area per bone surface (lesion area/BS).  $t_{(16)} = 5.472$ ,  $p < 0.0001$  by unpaired, two-tailed Student's  $t$  test. **B, J**, Representative  $\mu$ CT reconstruction images of sham and MM femurs at different time points; arrows indicate osteolysis. **C, K**, Percentage of cortical bone volume (BV). **D, L**, Percentage of trabecular bone volume per total volume (BV/TV). D17:  $t_{(16)} = 4.323$ ,  $p = 0.0005$ ; D24  $t_{(20)} = 4.107$ ,  $p = 0.0005$  by unpaired, two-tailed Student's  $t$  test. **E, M**, Percentage of trabecular bone surface per bone volume (BS/BV).  $t_{(16)} = 3.417$ ,  $p = 0.0035$  by unpaired, two-tailed Student's  $t$  test. **F, N**, Percentage of trabecular thickness (Tb.Th).  $t_{(16)} = 2.411$ ,  $p = 0.0283$  by unpaired, two-tailed Student's  $t$  test. **G, O**, Percentage of trabecular separation (Tb.Sp). D17:  $t_{(16)} = 3.903$ ,  $p = 0.0013$ ; D24:  $t_{(16)} = 6.381$ ,  $p < 0.0001$  by unpaired, two-tailed Student's  $t$  test. **H, P**, Percentage of trabecular number (Tb.N). D17  $t_{(16)} = 4.870$ ,  $p = 0.0002$ ; D24  $t_{(16)} = 5.228$ ,  $p < 0.0001$  by unpaired, two-tailed Student's  $t$  test. D = day. Sham  $n = 8-9$ ; MM  $n = 9-10$ .

2010) and breast (Bloom et al., 2011) bone metastases or osteosarcoma (Ghilardi et al., 2010; Mantyh et al., 2010). No micro-neuromas were observed in MM<sup>NP137</sup> mice. Systemic antibody treatment by itself in sham mice had no effect on behavior, bone structural parameters or neuronal innervation (data not shown), and pharmacokinetic analyses confirmed the presence of NP137 in the serum of all treated mice (Fig. 5E).

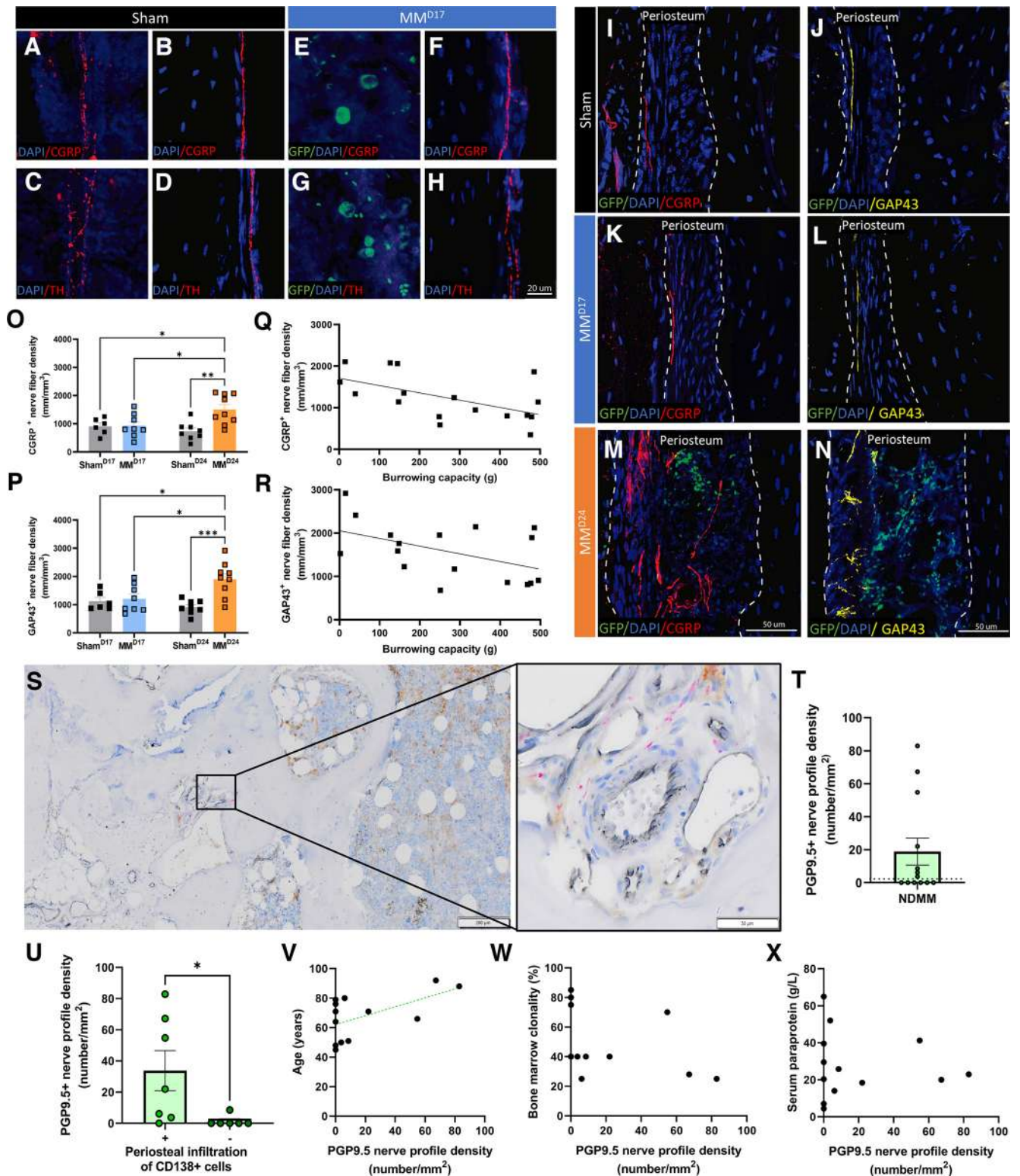
### Dorsal root ganglia (DRG) transcriptomic dysregulation reveals MM infiltration

Following our observation of periosteal sprouting at the onset of nociception, we next hypothesized that MM invasion of the bone niche induces transcriptomic changes in the cell bodies of the innervating nerve fibers. However, considering that blocking of the nerve fiber sprouting only had a transient analgesic effect, there are clearly other mechanisms involved in MIBP. To test this, the DRG transcriptomic signature of sham or 5TGM1-GFP inoculated mice during MIBP was evaluated. As expected, MM<sup>D24</sup> animals displayed nociception (Fig. 6A) and splenomegaly (Fig. 6B), confirming disease development. On postsurgical day 24, RNA from lumbar DRGs L2, L3, and L4 was extracted and sequenced (if RIN > 8), resulting in library sizes of 19–22 million reads per sample. The mapping rates to the mouse transcriptome were similar across samples, ranging between 88–92% of all reads. We identified 1389 differentially expressed genes (DEGs) between MM and sham groups with a

false discovery rate (FDR) < 5% (Fig. 6C,D). Interestingly, the DRG transcriptomic signature of MM mice was highly heterogeneous across samples; this heterogeneity was not correlated to tumor burden (Fig. 6D). However, significant changes in the expression pattern of DRG gene expression were driven by the presence and transcriptional level of green fluorescent protein (GFP; Fig. 6D), suggestive of MM infiltration to the DRG. Next, we performed gene set enrichment analyses (GSEA) to better interpret the transcriptional dysregulation by taking into account the entire set of genes expressed in our data and without setting up any arbitrary threshold of statistical significance on differential expression. GSEA for GO BP (Gene Ontology biological process) terms and Reactome pathways indicated that the main dysregulated signaling pathways in MM mice were related to cell cycle, immune response (activated) and neuronal signaling (suppressed; Extended Data Fig. 6-2).

Next, we compared the MIBP transcriptomic signature with that of six other models encompassing different painful conditions, as compiled previously (Bangash et al., 2018). These included (Fig. 6E) mouse models of painful lung cancer metastasis to the bone (cancer), partial sciatic nerve ligation (PSL), mechanical joint loading (MJL), chemotherapy induced peripheral neuropathy (Oxaliplatin), chronic muscle pain (CMP), and inflammation (complete Freund's adjuvant; CFA). To identify similarities among different painful conditions, we first examined the overlap between the set of MIBP DEGs, and the top 300





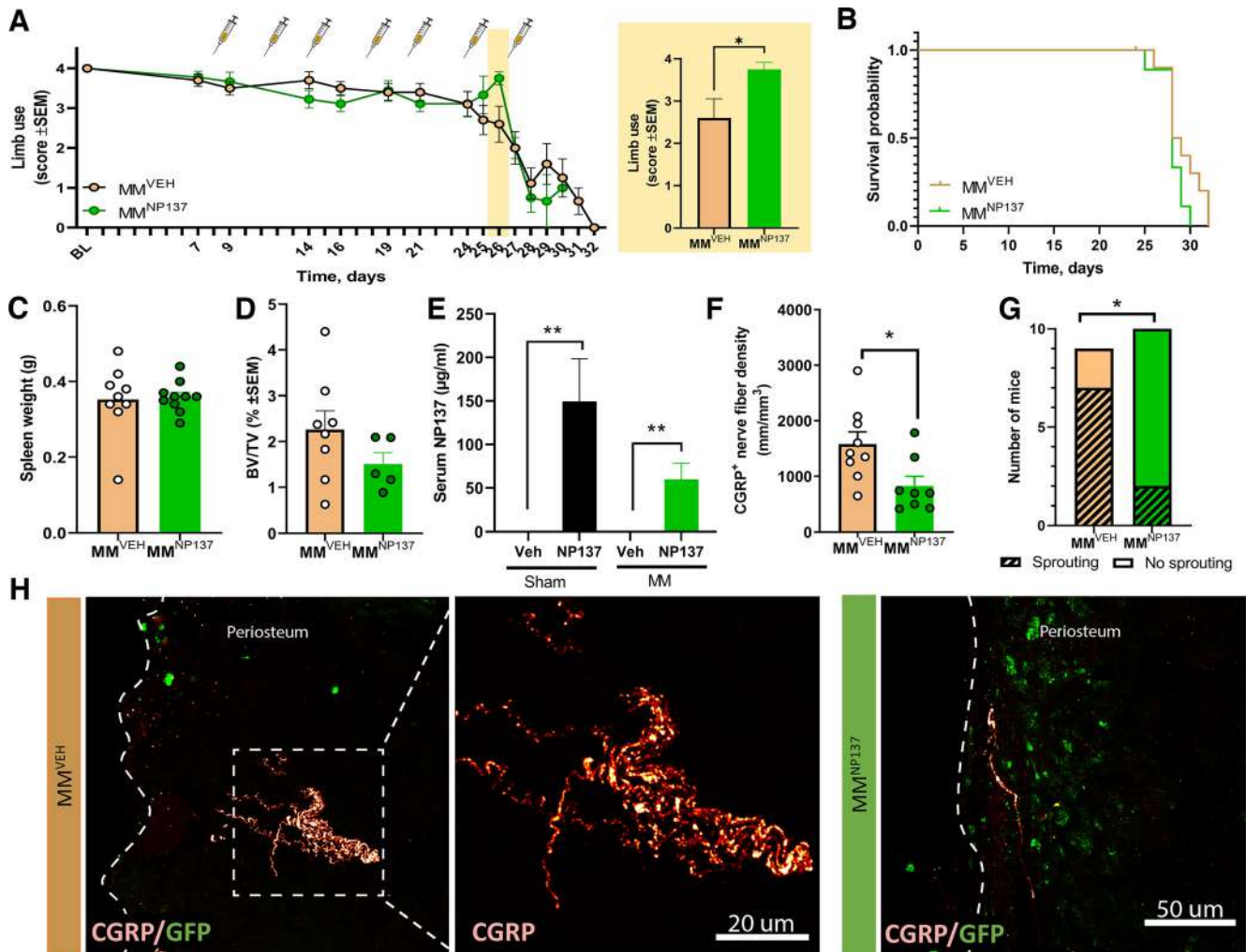


**Figure 5.** Pharmacological blockage of periosteal nerve sprouting delays the onset of pain-like behavior in 5TGM1-bearing mice. **A**, Effect of anti-netrin-1 treatment (NP137 10 mg/kg, i.p.; dosing days represented by syringes) on myeloma-bearing mice; exert indicates limb use scores on postsurgical day 26 (onset of pain-like behavior).  $t_{(16)} = 2.164$ ,  $p = 0.0451$  by unpaired, two-tailed Student's *t* test. **B**, Kaplan–Meier curve of vehicle- and NP137-treated MM mice. **C**, Endpoint spleen weight. **D**, Effect of systemic NP137 treatment on bone osteolysis, measured as bone volume per total volume (BV/TV). **E**, Serum concentration of NP137.  $F_{(1,22)} = 18.66$ ,  $p = 0.0003$ ; Sham ( $n = 4$ ): veh versus NP137  $p = 0.0015$ ; MM ( $n = 8/9$ ): veh versus NP137  $p = 0.0015$  by two-way ANOVA followed by Tukey's *post hoc* test. **F**, Quantification of CGRP<sup>+</sup> periosteal nerve density.  $t_{(15)} = 2.63$ ,  $p = 0.0188$  by unpaired, two-tailed Student's *t* test. **G**, Number of vehicle- or NP137-treated MM mice presenting periosteal nerve sprouting.  $\chi^2(1) = 6.343$ ,  $p = 0.0118$  by  $\chi^2$  test. **H**, Representative images of periosteal CGRP<sup>+</sup> nerve fibers and GFP<sup>+</sup> MM cells in MM mice treated with vehicle or NP137. MM = multiple myeloma. MM<sup>VEH</sup>  $n = 9$ , MM<sup>NP137</sup>  $n = 10$ .

genes with smallest *p*-values from each of the six conditions. Our analyses indicate that MIBP has most DEGs congruent with the PSL and CFA models, suggesting a neuropathic and an inflammatory component (Fig. 6E).

Next, we performed GSEA for the six models and compared results by selecting the top 40 enriched GO BP terms or Reactome pathways in MIBP and visualizing their normalized enrichment score and corresponding adjusted *p*-values across all models (Fig. 6F; Extended Data Fig. 6-2). Interestingly, the transcriptional signature of MM was overall most similar to that of PSL, suggesting a strong neuropathic component in MIBP. These results are in line with our previous finding of periosteal nerve sprouting as a contributing mechanism to MIBP. Although the overlap of DEGs is higher with the CFA model, the comparative GSEA analysis indicates that this similarity is only retained at the level of common activated inflammation-related pathways. Since spinal microglial reaction is a well-known feature of neuropathic pain (Chen et al., 2018; Inoue and Tsuda, 2018), we characterized the expression of ionized calcium-binding adaptor molecule 1 (Iba1) and phospho-p38 mitogen-activated

protein kinase (P-p38 MAPK) in the dorsal horn of the spinal cord of sham<sup>D24</sup> and MM<sup>D24</sup> mice. No changes in relative Iba1<sup>+</sup> or Pp38<sup>+</sup> cell number were observed at any lumbar region (Fig. 7). Likewise, no changes in glial fibrillary acidic protein (GFAP) staining were observed, suggesting that astrocytosis is not a main feature of MIBP (Fig. 7).

#### MM infiltration and increased ATF3 expression in DRGs from MM<sup>D24</sup> mice

To further verify that the GFP reads detected during transcriptome sequencing were caused by MM infiltration to the DRG and not the result of sample contamination, we performed immunofluorescent GFP staining on the ipsilateral DRGs of sham and MM bearing mice euthanized on postsurgical day 17 or 24 (Fig. 8A,B). We found 5TGM1-GFP infiltration in the ipsilateral L2 DRG of all MM<sup>D24</sup> mice confirming the results from the transcriptomic analysis (Fig. 8C). Similar results were found in the ipsilateral L3 (data not shown). No GFP expression was detected in DRGs of MM<sup>D17</sup> and sham controls (Fig. 8B,C). Thus, our data indicate that MM has the capacity to metastasize to the

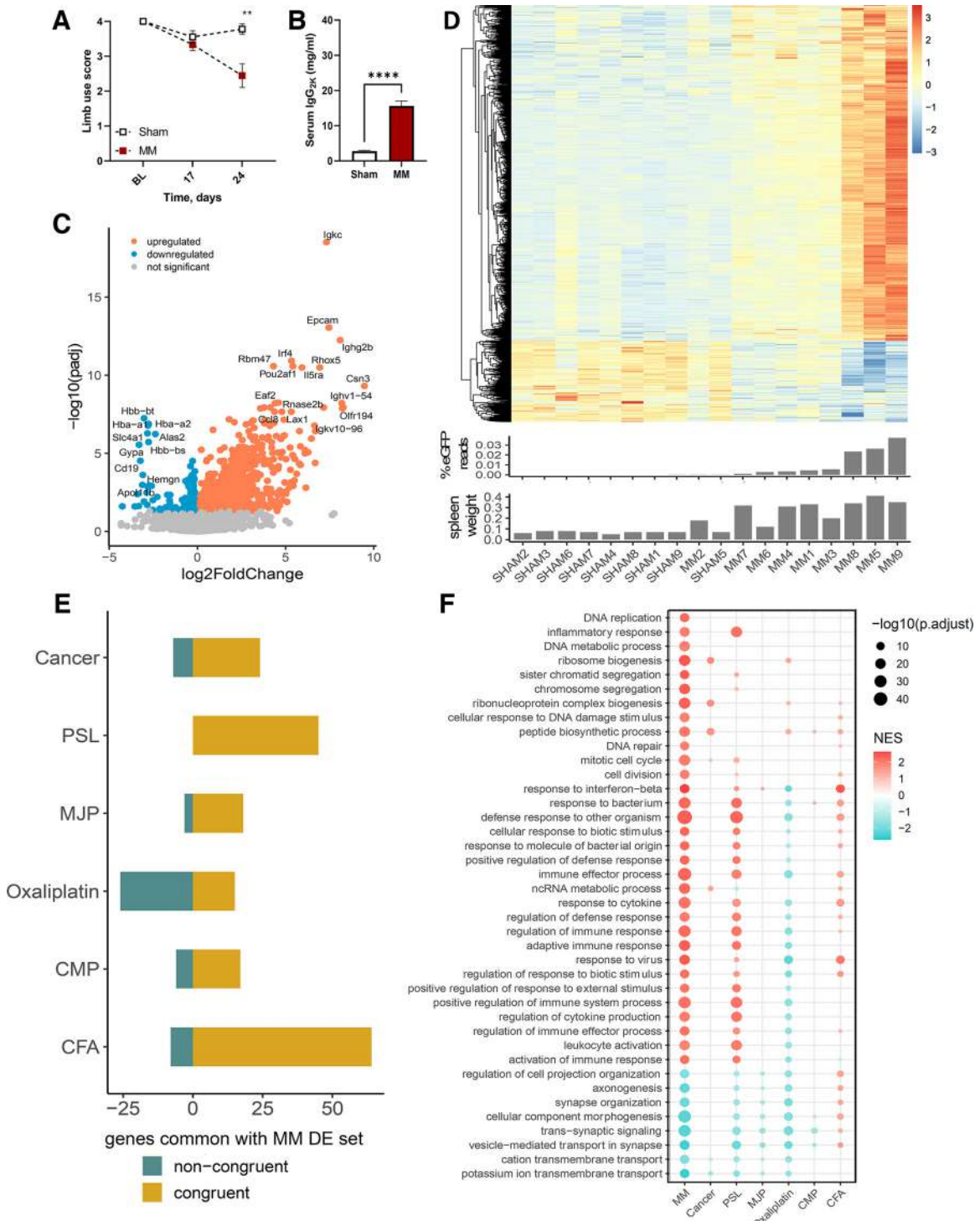


**Figure 6.** The DRG transcriptional signature in MM unveils MM infiltration to the nervous system and a strong neuropathic component. **A, B**, Development of nociception (**A**) and splenomegaly (**B**) were confirmed before DRG isolation and transcriptomic analyses.  $F_{(1,36)} = 0.0127$ ;  $D24 p = 0.0012$  by Friedman's two-way test followed by Wilcoxon's two-sample test and  $t_{(16)} = 9.106$ ,  $p < 0.0001$  by unpaired, two-tailed Student's  $t$  test. **C**, Volcano plot showing the log<sub>2</sub> fold change of differentially expressed genes (DEGs) between sham<sup>D24</sup> and MM<sup>D24</sup>. **D**, Heatmap depicting z-scaled regularized log counts of the 1389 DEGs identified between sham and MM lumbar DRGs (adjusted  $p$ -value  $< 0.05$ ). The heterogeneous transcriptome of MM DRG was correlated to the presence and levels of GFP expression. **E**, Comparison to other mouse pain models in terms of common DEGs. The overlap between the DEGs identified in MM mice and top 300 DEGs, sorted by  $p$ -value, in other painful models, as reported previously (Bangash et al., 2018), highlights the neuropathic and inflammatory component of MIBP. In yellow, common DEGs congruent in their direction of regulation between MM and each of the other models; in blue, common DEGs in noncongruent direction of regulation; raw data available in Extended Data Figure 6-1. **F**, Model comparison in terms of GSEA. Normalized enrichment scores (NES) and their corresponding  $p$ -values for the top 40 enriched GO terms in MIBP are displayed across all seven pain models (Bangash et al., 2018), indicating that the PSL model is the most similar to MIBP. Top 40 GO BP terms and top 40 enriched reactome pathways are displayed in Extended Data Figure 6-2. MM = multiple myeloma. PSL = partial sciatic nerve ligation. MJP = mechanical joint loading. CMP = chronic muscle pain. CFA = complete Freund's adjuvant. D = day. Sham  $n = 9$ ; MM  $n = 9$ .

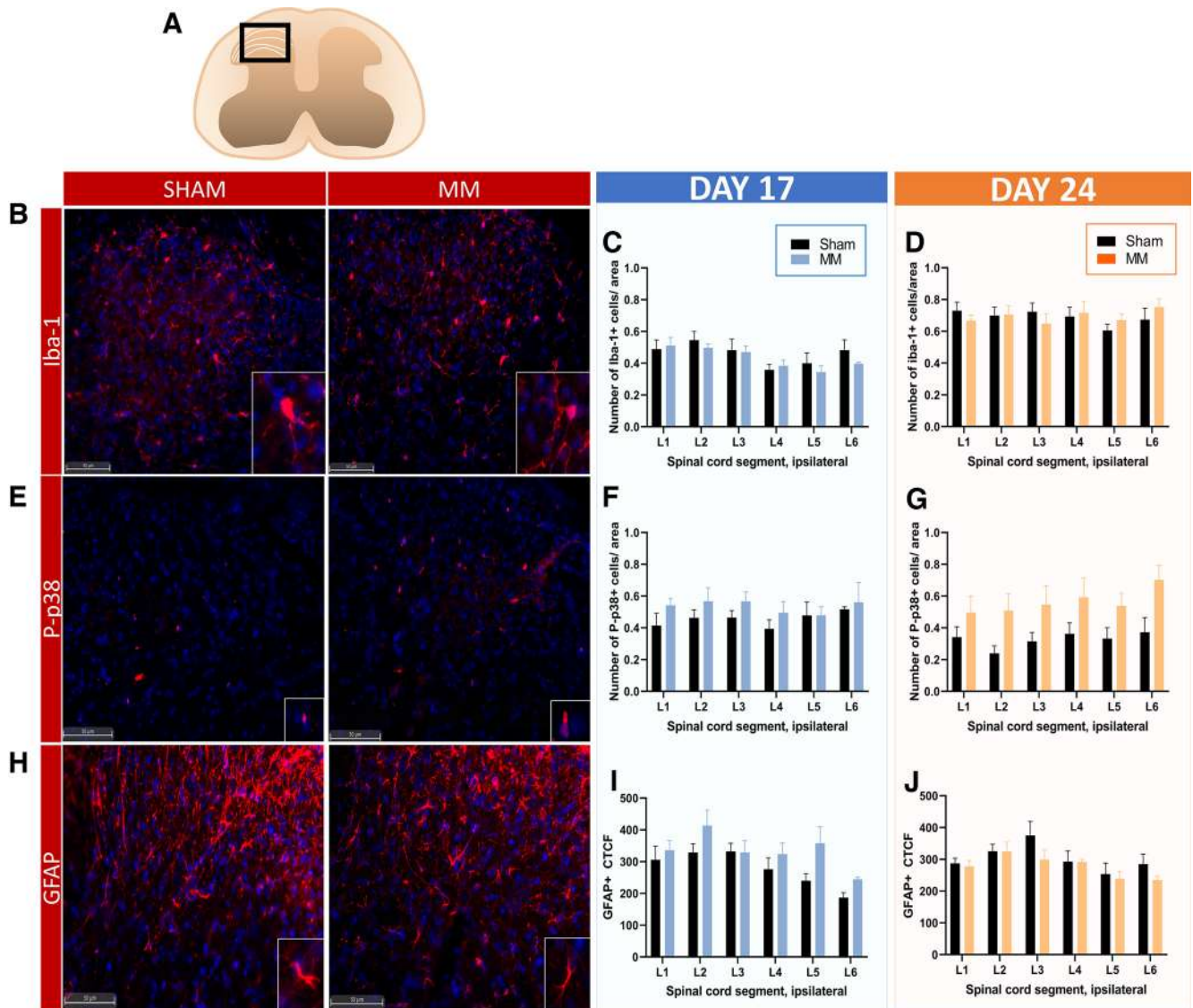


**Figure 7.** Microglia reaction and astrocytosis are not a main feature of MIBP. **(A)** Overview of the  $347 \times 260 \mu\text{m}^2$  area encompassing laminae I–IV of the dorsal horn in which Iba-1, P-p38 and GFAP were analysed. **(B, E, H)** Representative image of Iba-1<sup>+</sup> microglia cells **(B)**, Pp38<sup>+</sup> microglia cells **(E)** or GFAP<sup>+</sup> astrocytes **(H)** in the ipsilateral dorsal horn of the spinal cord. **(C, D, F, G)** The relative number of Iba-1<sup>+</sup> **(C, D)** or P-p38 **(F, G)** microglia cells in the ipsilateral dorsal horn of the spinal cord of lumbar regions L1 to L6 was unchanged between MM and sham mice euthanized on day 17 or 24. The area of Iba-1<sup>+</sup> immunoreactivity was also unchanged (data not shown). **(I, J)** The level of normalized GFAP expression in the dorsal horn of the spinal cord was similar between MM and sham mice euthanized on post-surgical day 17 or 24. L = lumbar. Data are analysed by 2-way repeated measure ANOVA and presented as mean  $\pm$  SEM. CTCF = Corrected Total Cell Fluorescence. Sham  $n = 6$ –8; MM  $n = 7$ –8.

peripheral nervous system, which occurs concomitantly to development of nociception.

Next, we examined the integrity of DRG vascularization and potential neuronal damage through immunofluorescent staining of the ipsilateral DRG of sham and MM mice 17 or 24 d after cell inoculation. Our analyses of CD31<sup>+</sup> blood vessels (Fig. 8D) revealed a significant decrease in blood vessel length (Fig. 8E–G) and density (Fig. 8H–J) in DRGs from MM<sup>D24</sup>, but not MM<sup>D17</sup>, compared with sham at all the analyzed lumbar levels. The proportion of sympathetic TH<sup>+</sup> neurons was similar across samples (Fig. 8L); however, the percentage of activating transcription factor 3 (ATF3)<sup>+</sup> neuron profiles was significantly increased in ipsilateral MM<sup>D24</sup> as compared with sham<sup>D24</sup>, suggesting tumor-induced neuronal injury (Fig. 8K,M). Additionally, ATF3 and 4',6-diamidino-2-phenylindole (DAPI) staining revealed a specific pattern of nuclear staining consistent with the development of Nageotte nodules, indicative of neuronal degeneration

(Peters et al., 2007; Fig. 8K). Finally, we examined the contralateral MM<sup>D24</sup> DRGs and found intact vasculature and low levels of ATF3 expression (data not shown), suggesting that MM DRG infiltration and concomitant vasculature and neuronal damage may be a specific mechanism of MIBP.

### The transcriptomic DRG signature of a MM patient suggests metastatic infiltration

Following our unexpected observation of MM metastasis to the DRG of myeloma-bearing mice displaying MIBP, we questioned the translational validity of our findings. To evaluate whether the genetic signature of MM cells was present in peripheral nervous system of a MM patient, we accessed the transcriptome of 68 DRGs collected from 39 patients with 18 different types of cancer (Ray et al., 2023), as well as that of two thoracic DRGs from one MM patient. Median age of the patient cohort was 60 years (spanning from 33 to 79 years) and 15 patients were females

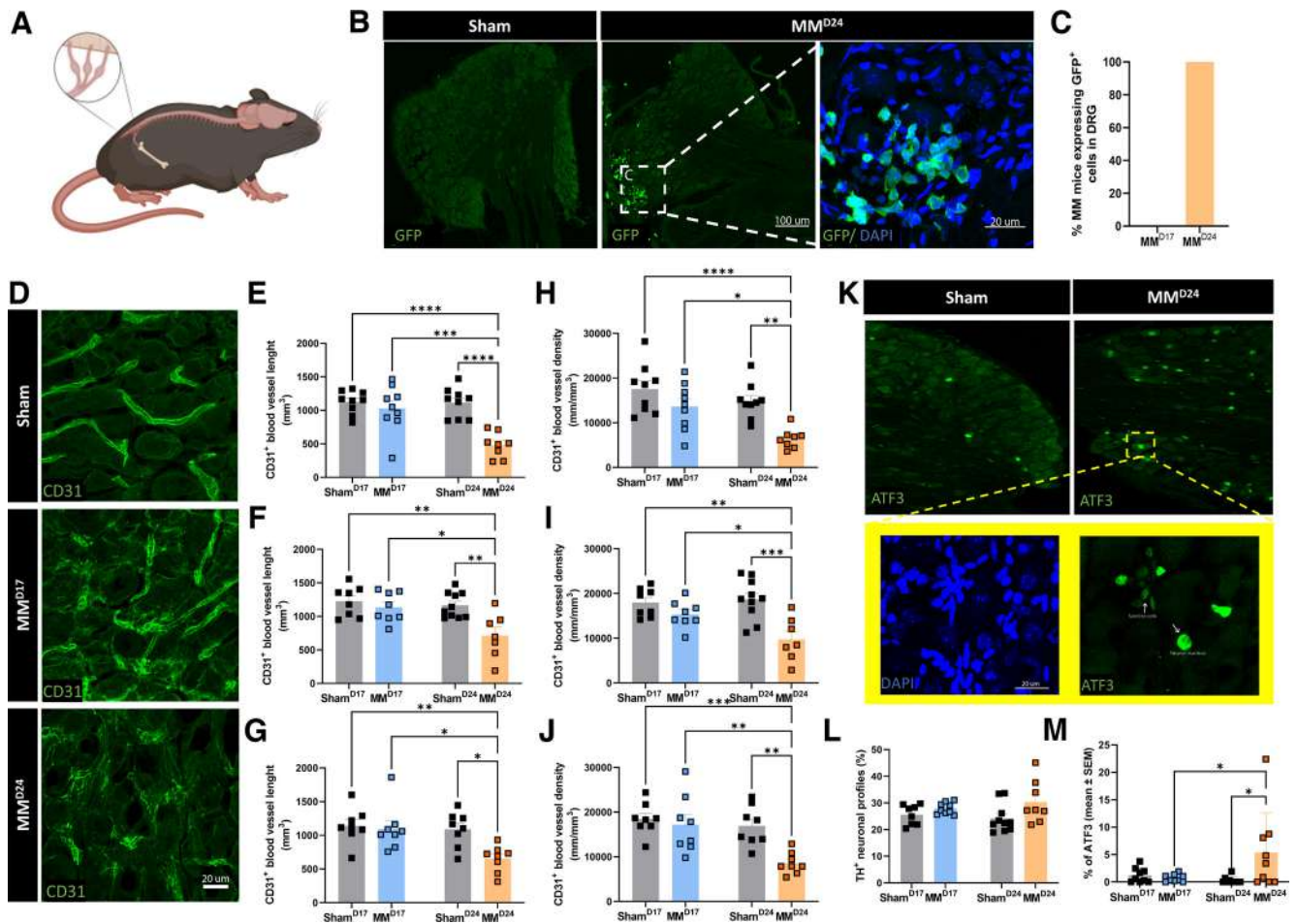


**Figure 8.** MM cells metastasize to the DRG causing damage to vasculature and neuronal bodies. **A**, Ipsilateral and contralateral lumbar DRGs L2, L3, and L4 were collected. **B**, Frozen sections from L3 DRGs were immunostained for GFP. **C**, Number of MM bearing mice presenting GFP<sup>+</sup> staining in the ipsilateral L3 DRG. **D**, Representative images of CD31<sup>+</sup> immunostaining in DRG frozen sections. Note the structural injury to CD31<sup>+</sup> blood vessels in MM<sup>D24</sup>, indicated by white arrows. **E–G**, Quantification of CD31<sup>+</sup> blood vessel length in the ipsilateral L2 (**E**), L3 (**F**), and L4 (**G**) DRGs. **E**,  $F_{(1,31)} = 10.57$ ,  $p = 0.0028$ , Sham<sup>D24</sup> versus MM<sup>D24</sup>,  $p = 0.0004$ ; MM<sup>D17</sup> versus MM<sup>D24</sup>,  $p < 0.0001$ ; sham<sup>D17</sup> versus MM<sup>D24</sup>,  $p < 0.0001$ . **F**,  $F_{(1,29)} = 4.610$ ,  $p = 0.0403$ , Sham<sup>D24</sup> versus MM<sup>D24</sup>,  $p = 0.0105$ ; MM<sup>D17</sup> versus MM<sup>D24</sup>,  $p = 0.0036$ ; sham<sup>D17</sup> versus MM<sup>D24</sup>,  $p = 0.0017$ . **G**,  $F_{(1,28)} = 4.321$ ,  $p = 0.0469$ , Sham<sup>D24</sup> versus MM<sup>D24</sup>,  $p = 0.0129$ ; MM<sup>D17</sup> versus MM<sup>D24</sup>,  $p = 0.0142$ ; sham<sup>D17</sup> versus MM<sup>D24</sup>,  $p = 0.0056$  by two-way ANOVA followed by Tukey's correction. **H–J**, Quantification of relative CD31<sup>+</sup> blood vessel density in the ipsilateral L2 (**H**), L3 (**I**), and L4 (**J**) DRGs. **H**,  $F_{(1,31)} = 2.214$ ,  $p = 0.1468$ , Sham<sup>D24</sup> versus MM<sup>D24</sup>,  $p = 0.0119$ ; MM<sup>D17</sup> versus MM<sup>D24</sup>,  $p = 0.0028$ ; sham<sup>D17</sup> versus MM<sup>D24</sup>,  $p < 0.0001$ . **I**,  $F_{(1,29)} = 5.178$ ,  $p = 0.0304$ , Sham<sup>D24</sup> versus MM<sup>D24</sup>,  $p = 0.0499$ ; MM<sup>D17</sup> versus MM<sup>D24</sup>,  $p = 0.0005$ ; sham<sup>D17</sup> versus MM<sup>D24</sup>,  $p = 0.0022$ . **J**,  $F_{(1,28)} = 10.31$ ,  $p = 0.0033$ , Sham<sup>D24</sup> versus MM<sup>D24</sup>,  $p = 0.0037$ ; MM<sup>D17</sup> versus MM<sup>D24</sup>,  $p = 0.0051$ ; sham<sup>D17</sup> versus MM<sup>D24</sup>,  $p = 0.008$  by two-way ANOVA followed by Tukey's *post hoc* test. **L**, TH<sup>+</sup> quantification in frozen sections from L2 DRGs. **K**, ATF3<sup>+</sup> immunoreactivity; exert denotes high-resolution imaging of ATF3<sup>+</sup> and DAPI immunoreactivity on ipsilateral L2 MM<sup>D24</sup> DRG. Note the presence of Nageotte nodules denoted with white arrows, suggestive of neuronal degeneration. **M**, ATF3<sup>+</sup> quantification in L3 DRGs.  $F_{(1,33)} = 5.363$ ,  $p = 0.0269$ ; Sham<sup>D24</sup> versus MM<sup>D24</sup>,  $p = 0.0492$ ; MM<sup>D17</sup> versus MM<sup>D24</sup>,  $p = 0.0239$  by two-way ANOVA followed by Tukey's *post hoc* test. MM = multiple myeloma. Sham  $n = 8–9$ ; MM  $n = 7–10$ .

(35.58%); detailed patient characteristics have previously been reported (Ray et al., 2023). First, we used publicly available datasets to generate a transcriptomic signature of composed of human markers generally expressed in MM cells (Zhan et al., 2006; Jang et al., 2019; Barwick et al., 2021) that show low or no expression in healthy DRG tissue (Ray et al., 2018). Datasets were chosen to represent different high throughput technologies (Affymetrix, bulk RNA-seq and single cell RNA-seq) and the final MM signature contained 40 genes that were ranked within the top 10,000 genes in Affymetrix and bulk-RNA, detected in over a third of single-cell RNA-seq cells, and had an expression rank  $< 0.75$  TPM in normal DRG tissue. Gene expression of the 40 signature markers was generally higher in the DRGs of the MM patient compared with most other cancer samples (Fig. 9A). Indeed, the distribution of percentile gene expression of the two MM samples over the other cancer samples, across the 40 MM markers, showed a general shift toward higher percentiles (Fig. 9B), with a mean percentile of 71.6 (mean of the two samples

from the MM patient). In order to check whether other cancer samples displayed a similarly high or higher MM signature, we plotted the mean percentile marker distribution for all other 68 cancer samples and confirmed that MM samples showed among the highest mean percentile (Fig. 9C). Other samples with a high mean percentile (indicative of similarly enriched expression of the selected marker genes) were DRGs from prostate and renal cell carcinoma patients (Extended Data Fig. 9-1).

Next, we asked whether the MIBP transcriptomic signature identified in our animal experiments was translatable to the human condition. Since the DEGs observed in MM<sup>D24</sup> versus sham<sup>D24</sup> mice seemed to be largely driven by MM cell infiltration to the DRG, we hypothesized that these DEGs are either expressed in MM cells or disrupted as a result of MM infiltration and could be used as a proxy for MM metastasis in patient data. Thus, we selected the set of human orthologs to the mouse up-regulated DEGs ( $padj < 0.05$ ) in MM<sup>D24</sup>, resulting in a set of 797

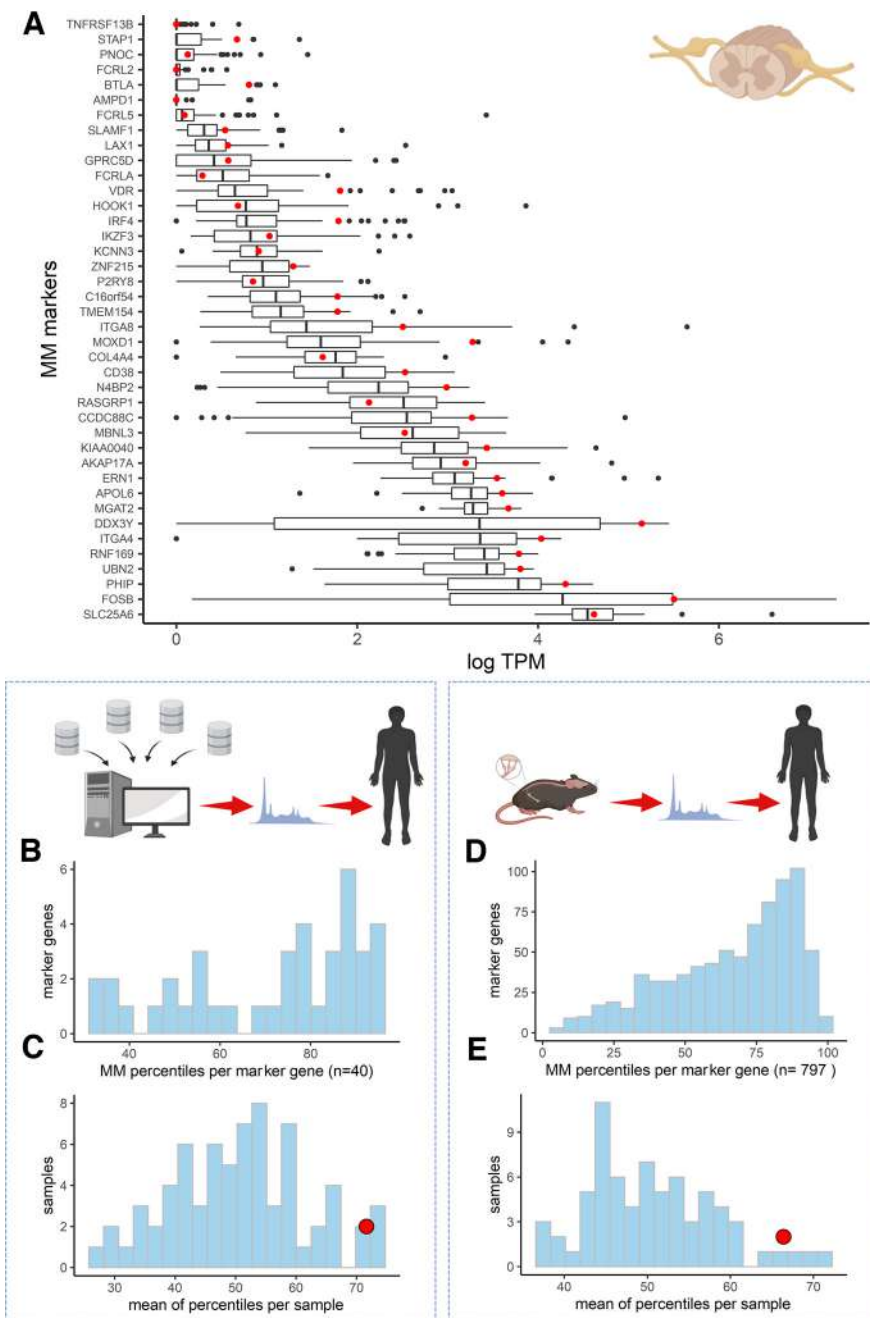


**Figure 9.** The transcriptomic signature of a MM patient suggests cancer infiltration to the DRG. **A**, Box-plot of log FPKM counts for the 40 signature MM markers across 70 DRGs from cancer patients. Red dots indicate the mean expression level in two thoracic DRGs from one MM patient. **B**, Distribution of percentile gene expression for all 40 markers in the DRGs of the MM patient. **C**, Distribution of mean percentiles across all cancer samples; red dot indicates the mean percentile for the MM patient. **D**, Distribution of percentile gene expression for the signature set derived from the mouse MM<sup>D24</sup> upregulated DEGs (*padj* < 0.05). **E**, Distribution of mean percentiles across all cancer samples; red dot indicating the mean percentile for the MM patient, for the mouse MM<sup>D24</sup>-derived set. Raw data available in Extended Data Figure 9-1.

genes. Like with the human datasets, the relative gene expression of the chosen markers displayed a distribution shift toward higher percentiles, indicating a tendency toward overexpression of the genes from this set in the human MM DRGs compared with other cancers (Fig. 9D). The MM samples showed among the highest mean percentile (mean of the two MM samples, 66.4; Fig. 9E). Taken altogether, our data suggest that cancer metastasis to the DRG may also occur in MM patients.

## Discussion

Bone pain remains among the main complaints from MM patients and significantly impairs their quality of life; indeed, previous reports have highlighted that MM patients report more symptoms and problems than leukemia and lymphoma patients (Johnsen et al., 2009). However, the preclinical search for adequate analgesic options for MIBP is scarce and pathophysiological mechanisms underlying bone cancer pain are poorly understood (Hiasa et al., 2017; Olechnowicz et al., 2019; Diaz-delCastillo et al., 2020b).

In this study, we use our previously characterized local immunocompetent mouse model of MIBP (Diaz-delCastillo et al., 2020b) to investigate disease-driven alterations of the central and peripheral nervous system that may lead to rational search of new analgesic targets. Following 5TGM1-GFP cell transplantation into the intrafemoral marrow of a tumor-permissive mouse strain, we observed the progressive development of nonstimulus evoked nociceptive behaviors that can be considered as surrogate markers of spontaneous pain and/or wellbeing (Deacon, 2006; Slieden et al., 2019). Behavioral tests and experimental time points (i.e., collection of tissue on postsurgical day 17 or 24) were selected according to our previous model characterization (Diaz-delCastillo et al., 2020b). Indeed, we have previously shown that systemic opioid administration (10 mg/kg morphine) on postsurgical day 26 reverses the MM induced deficits in limb use, further confirming model validity (Diaz-delCastillo et al., 2020b).

Following the direct transplantation of 5TGM1-GFP cells into a permissive microenvironment, we observed trabecular bone loss as early as postsurgical day 17, before the development of nociception. This apparent disconnection between osteolytic damage and nociception is consistent with preclinical and clinical evidence highlighting the limited analgesic efficacy of commonly used anti-resorptive treatments such as bisphosphonates (Mhaskar et al., 2017; Porta-Sales et al., 2017; Coluzzi et al., 2019; Diaz-delCastillo et al., 2020b). In contrast, we observed cortical osteolysis at later stages of the disease, coinciding with the onset of nociception and suggesting periosteal involvement in MIBP. To confirm this, further immunostaining demonstrated 5TGM1-GFP cell escape to the periosteum of these bones, along with significant sprouting of sensory neurons, concomitant to nociception. Periosteal nerve sprouting has been posed as a potential mechanism of cancer-induced bone pain in animal models of breast (Bloom et al., 2011) and prostate bone metastasis (Jimenez-Andrade et al., 2010), as well as osteosarcoma (Mantyh et al., 2010), and anti-NGF therapy has recently

showed modest results for the treatment of cancer pain (Sopata et al., 2015). Our results support the hypothesis that myeloma cells cause osteolytic cortical lesions through which they escape to the periosteum, where they may release neurotrophic factors that promote nerve sprouting and, potentially, nociception. The translational implication of these preclinical results is further supported by our exploratory observation of increased periosteal nerve density in NDMM patients compared with patients with hyperparathyroidism (Sayilekshmy et al., 2019), and the observation that periosteal nerve sprouting occurred more frequently in patients with periosteal infiltration of MM cells. Future studies addressing periosteal nerve sprouting in patients with MM and healthy controls are needed to confirm our findings.

To evaluate the contribution of periosteal nerve sprouting to MIBP, we tested the effect of repeated systemic NP137 administration. NP137 is a humanized monoclonal antibody targeting Netrin-1 that is currently undergoing Phase I and II clinical trials (NCT02977195; NCT04652076) as an anti-cancer treatment. Because Netrin-1 is a neurotrophic ligand involved in axon guidance, we expected that NP137 treatment would prevent periosteal nerve sprouting and, consequently, MIBP. Our results demonstrated that netrin-1 blockage effectively prevents periosteal nerve sprouting in myeloma-bearing mice without affecting bone morphometry. In contrast to previous studies (Fahed et al., 2022), systemic NP137 administration failed to have an effect of tumor burden or survival. While the reasons for this discrepancy are unknown, serum levels of sham drug-treated mice were twice as high compared with those of MM drug-treated mice, suggesting increased antibody clearance and volume distribution in MM-bearing mice. Future studies with greater doses of this antibody in mice with MM are warranted to determine its effect on tumor and disease progression.

Next, we evaluated the transcriptional DRG signature of MIBP and compared it to that of other pain models, including bone cancer metastasis, peripheral neuropathy, inflammation and chemotherapy-induced bone pain, as previously described (Bangash et al., 2018). Our data suggested that the transcriptional signature of MM bone pain was more similar to that of neuropathic and inflammatory pain than to the other pain models. While it has been speculated that central-acting agents targeting sensitization (i.e., gabapentin and antidepressants) may pose an alternative for the management of MIBP (Coluzzi et al., 2019); there is a lack of evidence supporting this treatment line. Detailed examination of the spinal cord in MM and sham mice revealed neither microglia activation nor astrocyte reaction in the dorsal horn of the spinal cord at any investigated time point. However, our analyses of microglial reaction and astrocytosis were restricted to the spinal cord, and further research should investigate whether glial cells infiltrate to the DRG during MIBP. Moreover, central sensitization may occur without astrocytic or glial involvement, and we and others have previously reported that spinal microglial reaction in cancer-induced bone pain models is a highly variable occurrence that may not reflect the clinical reality (Honore et al., 2000; Diaz-delCastillo et al., 2020a). Instead, the neuropathic component of MIBP is in line with clinical reports describing baseline peripheral neuropathy in a proportion of MM patients (Richardson et al., 2012; Oortgiesen et al., 2022), which is also used as a prognostic factor of chemotherapy induced peripheral neuropathy and treatment outcome in this patient population (Dong et al., 2022). These results, in combination with our observation of periosteal nerve sprouting, suggest that medications targeted to neuropathic pain patients may be useful to treat a fraction of myeloma bone pain patients. However, our

approach has several limitations, including that the GSEA comparison between our MM model and those described previously (Bangash et al., 2018) is directly impacted by the quality of the data from each of the models. Thus, while the PSL model was the most similar to MM, it was also the one showing the highest statistical significance for the DEG analysis and resulted also in a higher number of significant GSEA terms; in contrast, cancer, CMP and MJP models (i.e., those with the lowest degree of similarity to MM) showed no DEGs falling within the threshold after FDR correction for the models, which may hinder the significance of our findings. Another important limitation is that all our analyses are restricted to male mice; this choice was informed by the higher prevalence of MM in males than females. However, the reasons underlying this disparity are unknown, and future studies should address the potential intersex variability in this mouse model (Bird et al., 2021).

Among the most important findings from our mouse transcriptomics analyses was the high heterogeneity in the pattern of DEG in MM mice. Interestingly, the MIBP transcriptional signature was not correlated to surrogate markers of tumor burden or nociception but was instead highly dependent on the number of GFP counts. These results strongly suggest MM metastases to the ganglia, a never-before described feature of the disease that we further confirmed through immunohistological staining. Along with the spatial localization of MM cells in the ganglia, we observed structural damage and reductions in length and density of blood vessels innervating the lumbar ganglia. Whether damage to the blood vessels occurs before neoplastic infiltration (thus allowing the passage of MM cells into the DRG) or is a consequence of it, remains to be elucidated. In any case, neoplastic infiltration of the ganglia occurs concomitant to neuronal damage, as demonstrated by the increase in ATF3<sup>+</sup> nerve profiles and the formation of nodules of Nagoette (Peters et al., 2007). This novel observation of neuronal degeneration at the onset of MIBP presents a new research avenue that requires further research to identify potential treatment targets; future studies could address the mechanisms of MM metastasis to the DRG and the involvement of immunomodulators in DRG colonization.

Our human transcriptomic analyses revealed a similar indication of possible neoplastic infiltration in the DRGs of a MM patient. To our knowledge, the only previous publication addressing this question is from 1958, when Dickenman and Chason (1958) found degenerative changes but no cancer infiltration in the DRGs of eight deceased MM patients. In contrast, we have performed bulk sequencing of two thoracic DRGs from a MM patient and compared our transcriptomic results to those of 39 patients with other cancer types. Comparing our custom-made MM transcriptional signature composed by MM genes with low or no expression in healthy DRG as per publicly available datasets to the gene expression profile of all 70 DRGs suggested that MM gene expression was enriched in the DRGs from the MM patient. Similarly, evaluating the expression pattern of human orthologs to DEG identified in MIBP mice revealed enrichment in the MM patient DRGs. This observational data supports the translational validity of our findings with the obvious limitation of the highly restricted sample number. Accessing quality human DRG tissue is challenging, but further research is needed to conclude whether cancer metastasis to the DRG is indeed a common occurrence in MM patients.

In conclusion, our data suggests that MIBP is mediated by concomitant mechanisms including periosteal nerve sprouting and neoplastic infiltration of the DRG. Moreover, the

transcriptional signature of MIBP indicates a neuropathic component and pain management in MM patients may require a multitargeted approach that include drugs targeting neuropathic pain.

## References

- Ansari N, Müller S, Stelzer EHK, Pampaloni F (2013) Quantitative 3D cell-based assay performed with cellular spheroids and fluorescence microscopy. *Methods Cell Biol* 13:295–309.
- Bangash MA, Alles SRA, Santana-Varela S, Millet Q, Sikandar S, de Clauser L, Ter Heegde F, Habib AM, Pereira V, Sexton JE, Emery EC, Li S, Luiz AP, Erdos J, Gossage SJ, Zhao J, Cox JJ, Wood JN (2018) Distinct transcriptional responses of mouse sensory neurons in models of human chronic pain conditions. *Wellcome Open Res* 3:78.
- Barwick BG, Gupta VA, Matulis SM, Patton JC, Powell DR, Gu Y, Jaye DL, Conneely KN, Lin YC, Hofmeister CC, Nooka AK, Keats JJ, Lonial S, Vertino PM, Boise LH (2021) Chromatin accessibility identifies regulatory elements predictive of gene expression and disease outcome in multiple myeloma. *Clin Cancer Res* 27:3178–3189.
- Bird S, Cairns D, Menzies T, Boyd K, Davies F, Cook G, Drayson M, Gregory W, Jenner M, Jones J, Kaiser M, Owen R, Jackson G, Morgan G, Pawlyn C (2021) Sex differences in multiple myeloma biology but not clinical outcomes: results from 3894 patients in the myeloma XI trial. *Clin Lymphoma Myeloma Leuk* 21:667–675.
- Bloom AP, Jimenez-Andrade JM, Taylor RN, Castañeda-Corral G, Kaczmarek MJ, Freeman KT, Coughlin KA, Ghilardi JR, Kuskowski MA, Mantyh PW (2011) Breast cancer-induced bone remodeling, skeletal pain, and sprouting of sensory nerve fibers. *J Pain* 12:698–711.
- Bouxein ML, Boyd SK, Christiansen BA, Guldberg RE, Jepsen KJ, Müller R (2010) Guidelines for assessment of bone microstructure in rodents using micro-computed tomography. *J Bone Miner Res* 25:1468–1486.
- Boyer NP, Gupton SL (2018) Revisiting Netrin-1: one who guides (axons). *Front Cell Neurosci* 12:221.
- Bushnell B (2021) BBMAP. Available at: <https://sourceforge.net/projects/bbmap/>.
- Chartier SR, Mitchell SA, Majuta LA, Mantyh PW (2018) The changing sensory and sympathetic innervation of the young, adult and aging mouse femur. *Neuroscience* 387:178–190.
- Chen G, Zhang Y-Q, Qadri YJ, Serhan CN, Ji R-R (2018) Microglia in pain: detrimental and protective roles in pathogenesis and resolution of pain. *Neuron* 100:1292–1311.
- Coluzzi F, Rolke R, Mercadante S (2019) Pain management in patients with multiple myeloma: an update. *Cancers* 11:2037.
- Cunningham F, et al. (2022) Ensembl 2022. *Nucleic Acids Res* 50:D988–D995.
- Dai M, Wang P, Boyd AD, Kostov G, Athey B, Jones EG, Bunney WE, Myers RM, Speed TP, Akil H, Watson SJ, Meng F (2005) Evolving gene/transcript definitions significantly alter the interpretation of GeneChip data. *Nucleic Acids Res* 33:e175.
- Davis S, Meltzer PS (2007) GEOquery: a bridge between the Gene Expression Omnibus (GEO) and BioConductor. *Bioinformatics* 23:1846–1847.
- Deacon RM (2006) Burrowing in rodents: a sensitive method for detecting behavioral dysfunction. *Nat Protoc* 1:118–121.
- Devor M, Wall PD (1976) Type of sensory nerve fibre sprouting to form a neuroma. *Nature* 262:705–708.
- Diaz-delCastillo M, Christiansen SH, Appel CK, Falk S, Woldbye DPD, Heegaard AM (2018) Neuropeptide Y is up-regulated and induces antinociception in cancer-induced bone pain. *Neuroscience* 384:111–119.
- Diaz-delCastillo M, Hansen RB, Appel CK, Nielsen L, Nielsen SN, Karynotakis K, Dahl LM, Andreasen RB, Heegaard AM (2020a) Modulation of rat cancer-induced bone pain is independent of spinal microglia activity. *Cancers* 12:2740.
- Diaz-delCastillo M, Kamstrup D, Olsen RB, Hansen RB, Pembridge T, Simanskaite B, Jimenez-Andrade JM, Lawson MA, Heegaard AM (2020b) Differential pain-related behaviors and bone disease in immunocompetent mouse models of myeloma. *JBMR Plus* 4:e10252.
- Dickenman RC, Chason JL (1958) Alterations in the dorsal root ganglia and adjacent nerves in the leukemias, the lymphomas and multiple myeloma. *Am J Pathol* 34:349–361.
- Dong M, Zhang J, Han X, He J, Zheng G, Cai Z (2022) Baseline peripheral neuropathy was associated with age and a prognostic factor in newly diagnosed multiple myeloma patients. *Sci Rep* 12:10061.
- Dun XP, Parkinson DB (2017) Role of Netrin-1 signaling in nerve regeneration. *Iran J Med Sci* 18:491.
- Fahed D, Chettab A, Mathe D, Denis M, Traverse-Glehen A, Karlin L, Perrial E, Dumontet C (2022) Netrin-1 expression and targeting in multiple myeloma. *Leuk Lymphoma* 63:395–403.
- Frankish A, et al. (2019) GENCODE reference annotation for the human and mouse genomes. *Nucleic Acids Res* 47:D766–D773.
- Ghilardi JR, Freeman KT, Jimenez-Andrade JM, Mantyh WG, Bloom AP, Kuskowski MA, Mantyh PW (2010) Administration of a tropomyosin receptor kinase inhibitor attenuates sarcoma-induced nerve sprouting, neuroma formation and bone cancer pain. *Mol Pain* 6:87.
- Glaser J, Gonzalez R, Perreau VM, Cotman CW, Keirstead HS (2004) Neutralization of the chemokine CXCL10 enhances tissue sparing and angiogenesis following spinal cord injury. *J Neurosci Res* 77:701–708.
- Hiasa M, Okui T, Allette YM, Ripsch MS, Sun-Wada GH, Wakabayashi H, Roodman GD, White FA, Yoneda T (2017) Bone pain induced by multiple myeloma is reduced by targeting V-ATPase and ASIC3. *Cancer Res* 77:1283–1295.
- Hirakawa H, Okajima S, Nagaoka T, Kubo T, Takamatsu T, Oyamada M (2004) Regional differences in blood-nerve barrier function and tight-junction protein expression within the rat dorsal root ganglion. *Neuroreport* 15:405–408.
- Honore P, Rogers SD, Schwei MJ, Salak-Johnson JL, Luger NM, Sabino MC, Clohisey DR, Mantyh PW (2000) Murine models of inflammatory, neuropathic and cancer pain each generates a unique set of neurochemical changes in the spinal cord and sensory neurons. *Neuroscience* 98:585–598.
- Howe KL, et al. (2021) Ensembl 2021. *Nucleic Acids Res* 49:D884–D891.
- Inoue K, Tsuda M (2018) Microglia in neuropathic pain: cellular and molecular mechanisms and therapeutic potential. *Nat Rev Neurosci* 19:138–152.
- Ireland WP, Fletcher TF, Bingham C (1981) Quantification of microvasculature in the canine spinal cord. *Anat Rec* 200:102–113.
- Jang JS, Li Y, Mitra AK, Bi L, Abyzov A, van Wijnen AJ, Baughn LB, Van Ness B, Rajkumar V, Kumar S, Jen J (2019) Molecular signatures of multiple myeloma progression through single cell RNA-Seq. *Blood Cancer J* 9:2.
- Jimenez-Andrade JM, Herrera MB, Ghilardi JR, Vardanyan M, Melemedjian OK, Mantyh PW (2008) Vascularization of the dorsal root ganglia and peripheral nerve of the mouse: implications for chemical-induced peripheral sensory neuropathies. *Mol Pain* 4:10.
- Jimenez-Andrade JM, Bloom AP, Stake JI, Mantyh WG, Taylor RN, Freeman KT, Ghilardi JR, Kuskowski MA, Mantyh PW (2010) Pathological sprouting of adult nociceptors in chronic prostate cancer-induced bone pain. *J Neurosci* 30:14649–14656.
- Johnsen AT, Tholstrup D, Petersen MA, Pedersen L, Groenvold M (2009) Health related quality of life in a nationally representative sample of haematological patients. *Eur J Haematol* 83:139–148.
- Kazandjian D, Landgren O (2016) A look backward and forward in the regulatory and treatment history of multiple myeloma: approval of novel agents, new drug development, and longer patient survival. *Semin Oncol* 43:682–689.
- Kumar SK, Rajkumar SV, Dispenzieri A, Lacy MQ, Hayman SR, Buadi FK, Zeldenzust SR, Dingli D, Russell SJ, Lust JA, Greipp PR, Kyle RA, Gertz MA (2008) Improved survival in multiple myeloma and the impact of novel therapies. *Blood* 111:2516–2520.
- Kyle RA, Rajkumar SV (2009) Criteria for diagnosis, staging, risk stratification and response assessment of multiple myeloma. *Leukemia* 23:3–9.
- Lawson MA, Paton-Hough JM, Evans HR, Walker RE, Harris W, Ratnabalan D, Snowden JA, Chantry AD (2015) NOD/SCID-GAMMA mice are an ideal strain to assess the efficacy of therapeutic agents used in the treatment of myeloma bone disease. *PLoS One* 10:e0119546.
- Love MI, Huber W, Anders S (2014) Moderated estimation of fold change and dispersion for RNA-seq data with DESeq2. *Genome Biol* 15:550.
- Mach DB, Rogers SD, Sabino MC, Luger NM, Schwei MJ, Pomonis JD, Keyser CP, Clohisey DR, Adams DJ, O’Leary P, Mantyh PW (2002) Origins of skeletal pain: sensory and sympathetic innervation of the mouse femur. *Neuroscience* 113:155–166.



- Madison RD, Zomorodi A, Robinson GA (2000) Netrin-1 and peripheral nerve regeneration in the adult rat. *Exp Neurol* 161:563–570.
- Mantyh PW (2014) The neurobiology of skeletal pain. *Eur J Neurosci* 39:508–519.
- Mantyh WG, Jimenez-Andrade JM, Stake JJ, Bloom AP, Kaczmarek MJ, Taylor RN, Freeman KT, Ghilardi JR, Kuskowski MA, Mantyh PW (2010) Blockade of nerve sprouting and neuroma formation markedly attenuates the development of late stage cancer pain. *Neuroscience* 171:588–598.
- Martin CD, Jimenez-Andrade JM, Ghilardi JR, Mantyh PW (2007) Organization of a unique net-like meshwork of CGRP+ sensory fibers in the mouse periosteum: implications for the generation and maintenance of bone fracture pain. *Neurosci Lett* 427:148–152.
- Mercadante S (2018) Treating breakthrough pain in oncology. *Expert Rev Anticancer Ther* 18:445–449.
- Mhaskar R, Kumar A, Miladinovic B, Djulbegovic B (2017) Bisphosphonates in multiple myeloma: an updated network meta-analysis. *Cochrane Database Syst Rev* 12:Cd003188.
- Nicola P, Scaramucci L, Romani C, Giovannini M, Tendas A, Brunetti G, Cartoni C, Palumbo R, Vischini G, Siniscalchi A, de Fabritiis P, Caravita T (2010) Pain management in multiple myeloma. *Expert Rev Anticancer Ther* 10:415–425.
- Olechnowicz SWZ, Weivoda MM, Lwin ST, Leung SK, Gooding S, Nador G, Javaid MK, Ramasamy K, Rao SR, Edwards JR, Edwards CM (2019) Multiple myeloma increases nerve growth factor and other pain-related markers through interactions with the bone microenvironment. *Sci Rep* 9:14189.
- Oortgiesen BE, Kroes JA, Scholtens P, Hoogland J, Dannenberg-de Keijzer P, Siemes C, Jansman FGA, Kibbelaar RE, Veeger NJGM, Hoogendoorn M, van Roon EN (2022) High prevalence of peripheral neuropathy in multiple myeloma patients and the impact of vitamin D levels, a cross-sectional study. *Support Care Cancer* 30:271–278.
- Patro R, Duggal G, Love MI, Irizarry RA, Kingsford C (2017) Salmon provides fast and bias-aware quantification of transcript expression. *Nat Methods* 14:417–419.
- Peters CM, Ghilardi JR, Keyser CP, Kubota K, Lindsay TH, Luger NM, Mach DB, Schwei MJ, Sevcik MA, Mantyh PW (2005) Tumor-induced injury of primary afferent sensory nerve fibers in bone cancer pain. *Exp Neurol* 193:85–100.
- Peters CM, Jimenez-Andrade JM, Kuskowski MA, Ghilardi JR, Mantyh PW (2007) An evolving cellular pathology occurs in dorsal root ganglia, peripheral nerve and spinal cord following intravenous administration of paclitaxel in the rat. *Brain Res* 1168:46–59.
- Porta-Sales J, Garzón-Rodríguez C, Llorens-Torromé S, Brunelli C, Pigni A, Caraceni A (2017) Evidence on the analgesic role of bisphosphonates and denosumab in the treatment of pain due to bone metastases: a systematic review within the European Association for Palliative Care guidelines project. *Palliat Med* 31:5–25.
- Quinn B, Ludwig H, Bailey A, Khela K, Marongiu A, Carlson KB, Rider A, Seesagur A (2022) Physical, emotional and social pain communication by patients diagnosed and living with multiple myeloma. *Pain Manag* 12:59–74.
- Ramsenthaler C, Kane P, Gao W, Siegert RJ, Edmonds PM, Schey SA, Higginson IJ (2016) Prevalence of symptoms in patients with multiple myeloma: a systematic review and meta-analysis. *Eur J Haematol* 97:416–429.
- Ray P, Torck A, Quigley L, Wangzhou A, Neiman M, Rao C, Lam T, Kim JY, Kim TH, Zhang MQ, Dussor G, Price TJ (2018) Comparative transcriptome profiling of the human and mouse dorsal root ganglia: an RNA-seq-based resource for pain and sensory neuroscience research. *Pain* 159:1325–1345.
- Ray PR, Shiers S, Caruso JP, Tavares-Ferreira D, Sankaranarayanan I, Uhelski ML, Li Y, North RY, Tatsui C, Dussor G, Burton MD, Dougherty PM, Price TJ (2023) RNA profiling of human dorsal root ganglia reveals sex-differences in mechanisms promoting neuropathic pain. *Brain* 146:749–766.
- Richardson PG, et al. (2012) Management of treatment-emergent peripheral neuropathy in multiple myeloma. *Leukemia* 26:595–608.
- Rudjito R, Agalave NM, Farinotti AB, Baharpoor A, Martinez Martinez A, Islas EM, Panwar P, Brömme D, Barbier J, Marchand F, Mehlen P, Andersen TL, Andrade JM, Svensson CI (2021) Bone innervation and vascularization regulated by osteoclasts contribute to refractive pain-related behavior in the collagen antibody-induced arthritis model. *bioRxiv* 2004.2019.440384.
- Sacks D, et al. (2018) Multisociety consensus quality improvement revised consensus statement for endovascular therapy of acute ischemic stroke. *Int J Stroke* 13:612–632.
- Sayilekshmy M, Hansen RB, Delaisé JM, Rolighed L, Andersen TL, Heegaard AM (2019) Innervation is higher above bone remodeling surfaces and in cortical pores in human bone: lessons from patients with primary hyperparathyroidism. *Sci Rep* 9:5361.
- Sliepen SHJ, Diaz-Delcastillo M, Koriath J, Olsen RB, Appel CK, Christoph T, Heegaard AM, Rutten K (2019) Cancer-induced bone pain impairs burrowing behaviour in mouse and rat. *In Vivo* 33:1125–1132.
- Soneson C, Love MI, Robinson MD (2015) Differential analyses for RNA-seq: transcript-level estimates improve gene-level inferences. *F1000Res* 4:1521.
- Sopata M, Katz N, Carey W, Smith MD, Keller D, Verburg KM, West CR, Wolfram G, Brown MT (2015) Efficacy and safety of tanezumab in the treatment of pain from bone metastases. *Pain* 156:1703–1713.
- Sung JH, Mastro AR (1983) Aberrant peripheral nerves and microneuromas in otherwise normal medullas. *J Neuropathol Exp Neurol* 42:522–528.
- Watson C, Paxinos G, Kayalioglu G, Heise C (2009) Atlas of the mouse spinal cord. In: *The spinal cord*, Chap 16 (Watson C, Paxinos G, and Kayalioglu G, eds), pp 308–379. San Diego: Academic.
- Weidner N, Semple JP, Welch WR, Folkman J (1991) Tumor angiogenesis and metastasis—correlation in invasive breast carcinoma. *N Engl J Med* 324:1–8.
- Yu G (2019) Enrichplot: visualization of functional enrichment result. R package version 1.20.0. Available at: <https://yulab-smu.top/biomedical-knowledge-mining-book/>.
- Yu G, He QY (2016) ReactomePA: an R/Bioconductor package for reactome pathway analysis and visualization. *Mol Biosyst* 12:477–479.
- Yu G, Wang LG, Yan GR, He QY (2015) DOSE: an R/Bioconductor package for disease ontology semantic and enrichment analysis. *Bioinformatics* 31:608–609.
- Zhan F, Huang Y, Colla S, Stewart JP, Hanamura I, Gupta S, Epstein J, Yaccoby S, Sawyer J, Burington B, Anaissie E, Hollmig K, Pineda-Roman M, Tricot G, van Rhee F, Walker R, Zangari M, Crowley J, Barlogie B, Shaughnessy JD Jr (2006) The molecular classification of multiple myeloma. *Blood* 108:2020–2028.
- Zheng B, Li S, Xiang Y, Zong W, Ma Q, Wang S, Wu H, Song H, Ren H, Chen J, Liu J, Zhao F (2023) Netrin-1 mediates nerve innervation and angiogenesis leading to discogenic pain. *J Orthop Translat* 39:21–33.
- Zhu S, et al. (2019) Subchondral bone osteoclasts induce sensory innervation and osteoarthritis pain. *J Clin Invest* 129:1076–1093.